Received: 27 July 2023 | Revised: 16 November 2023 | Accepted: 28 November 2023

DOI: 10.1111/ffe.14217

ORIGINAL ARTICLE

FFEMS Fatigue & Fracture of Engineering Materials & Structures WILEY

Quantitative analysis of three-dimensional fatigue crack path selection in Mg alloy WE43 using high-energy X-ray diffraction microscopy

Duncan A. Greeley[1] | **Jacob F. Adams**[1] | **Peter Kenesei**[2] | **Ashley D. Spear**[3] | **John E. Allison**[1]

[1]Department of Materials Science and Engineering, University of Michigan, Ann Arbor, Michigan, USA

[2]Advanced Photon Source, Argonne National Laboratory, Lemont, Illinois, USA

[3]Department of Mechanical Engineering, University of Utah, Salt Lake City, Utah, USA

Correspondence

Duncan A. Greeley, Department of Materials Science and Engineering, University of Michigan, 2300 Hayward St. Rm 3062, Ann Arbor, MI 48109, USA.
Email: greeleyd@umich.edu

Funding information

U.S. Department of Energy (Office of Science, Office of Basic Energy Sciences), Grant/Award Number: DE-SC0008637; U. S. Department of Energy (Office of Science), Grant/Award Number: DE-AC02-06CH11357; National Science Foundation, Grant/Award Number: CMMI-1629660

Abstract

Fatigue short-cracks in Mg alloys display complex growth behavior due to high plastic anisotropy and crack path dependence on local microstructural features. In this study, the three-dimensional crystallography of short-crack paths in Mg alloy WE43 was characterized by mapping near-field high-energy X-ray diffraction microscopy (HEDM) reconstructed grain maps to high-resolution X-ray CT reconstructions of the fracture surfaces in the crack initiation and short-crack growth regions of six ultrasonic fatigue specimens. Crack–grain–boundary intersections were analyzed at 81 locations across the six crack paths. The basal intragranular, non-basal intragranular, or intergranular character of short-crack growth following each boundary intersection was correlated to crystallographic and geometric parameters of the trailing and leading grains, three-dimensional grain boundary plane, and advancing crack front. The results indicate that crack paths are dependent on the combined crystallographic and geometric character of the local microstructure, and crack path prediction can be improved by use of dimensionality reduction on subsets of high-linear-correlation microstructural parameters.

KEYWORDS

high cycle fatigue, high-energy X-ray diffraction, magnesium alloys, short-crack growth

Highlights

- Three-dimensional short-crack growth was characterized with near-field HEDM and X-ray CT.
- Intragranular crack growth character correlates to favorable alignment for slip activity.
- Intergranular crack growth displays low association to local crystallography.

- Short-crack path predictions can be improved through PCA of microstructural parameters.

1 | INTRODUCTION

Short-crack growth, or crack growth on length scales equivalent to local microstructural features, is an important component of the total fatigue lifetime of structural parts, particularly in the high and very high cycle regimes.[1] In comparison to long fatigue cracks, microstructurally short-crack paths and growth rates are sensitive to local lattice orientations, microstructure features, and micromechanical states.[2,3] Short-crack growth direction is further influenced by dislocation behavior ahead of the crack tip and the interaction between the advancing crack front (CF) and grain and phase boundaries, resulting in complex and tortuous growth paths. In Mg alloys, short-crack growth paths are particularly complicated due to anisotropic plastic deformation behavior and the ease of both intragranular crack propagation, or crack growth through grains, and intergranular crack propagation, or crack growth along grain boundaries. This multi-modal growth behavior provides a challenge when predicting short-crack growth during high cycle fatigue in Mg alloys. To improve accuracy of short-crack growth predictions, it is necessary to better understand the interrelated impact of multiple microstructural features on crack path selection.

Short-crack paths are correlated to plastic deformation ahead of the crack tip, and dislocation slip in Mg alloys occurs along four primary slip modes: basal $\{0001\}<11\bar{2}0>$, prismatic $\{10\bar{1}0\}$ $<11\bar{2}0>$, pyramidal I <a> $\{10\bar{1}1\}<10\bar{1}0>$, and pyramidal II <c+a> $\{11\bar{2}2\}<11\bar{2}3>$.[4] Plastic deformation in conventional Mg alloys is highly anisotropic due to strong processing textures and large ratios between the critical resolved shear stress (CRSS) of basal and non-basal slip[5]; however, alloying with rare-earth (RE) elements has been shown to both weaken deformation texture and reduce the CRSS ratio of the basal to prismatic and basal to pyramidal slip modes.[6–9] While RE alloying is beneficial for improving the strength and low-temperature formability of Mg alloys, the higher activity of non-basal slip modes provides additional favorable short-crack growth planes, leading to more tortuous crack growth and complicating crack path predictions.

Crack paths display complex three-dimensional structures and are influenced by both surface and subsurface microstructural features that are not fully resolved by conventional characterization techniques such as electron backscatter diffraction (EBSD) and electron microscopy. Recent advances in non-destructive characterization tools, including X-ray computed tomography (CT),[10–12] diffraction contrast tomography (DCT),[13] and high-energy X-ray diffraction microscopy (HEDM or 3DXRD),[14] have provided novel approaches for correlating the full three-dimensional microstructure surrounding an advancing crack to crack growth character. HEDM[15,16] and DCT[17] are synchrotron X-ray diffraction techniques by which three-dimensional grain structure, including crystallographic orientations, can be reconstructed non-destructively and correlated to high-resolution three-dimensional X-ray CT fracture surface maps. Early work by Herbig et al.[18] showed that the crystallography of a fracture surface could be mapped by combining synchrotron DCT and X-ray CT reconstructions in a Ti alloy Ti21S. King et al.[19] combined DCT and in-situ X-ray CT to correlate the growth rate of an advancing three-dimensional short-crack to differences in slip mode Schmid factors (SFs) in different grains, the twist angle between slip modes at grain boundaries, and the crystallography of fracture facets in RE strengthened Mg alloy Elektron 21. Oddershede et al.[20] further mapped the three-dimensional grain-average elastic stress field surrounding a growing crack in Mg alloy AZ31 using far-field HEDM (ff-HEDM), and Spear et al.[21] combined post-mortem near-field HEDM (nf-HEDM), X-ray CT, and surface marker band analysis to track the growth rate, geometry, and crystallographic character of short fatigue crack in Al alloy 6061. In situ subsurface short-crack initiation and growth has also been characterized in a Ni-based alloy and correlated to the local micromechanical fields surrounding an inclusion using combined nf-HEDM, ff-HEDM, and X-ray CT.[22,23] The intragranular crack paths in the Ni alloy were observed to be aligned with the most active slip systems in the grains leading the CF, and crack arrest and propagation correlated to variations in local micromechanical states. The impact of heterogeneities in the stress states of individual grains surrounding a growing subsurface short-crack was also correlated to crack closure mechanisms in an Ni alloy by combining ff-HEDM and X-ray CT.[24] The three-dimensional character of intergranular short-crack growth during hydrogen-assisted fracture has also been characterized in a Ni-based alloy using nf-HEDM, and crack arrest and deviation from nominally favorable facets was correlated to the crystallographic character of the grain boundaries ahead of the advancing

CF.[25] While these studies have developed and validated the use of novel reconstruction techniques for characterizing the relationship between three-dimensional short-crack paths and local microstructural features and stress states in a range of alloys, the mechanisms underlying the complex short-crack path behavior observed in Mg alloys are still not well understood.

In this study, three-dimensional fatigue short-crack paths were characterized post-mortem in commercial RE-strengthened Mg alloy WE43 using nf-HEDM and synchrotron X-ray CT. The benefits of ex situ mechanical testing and post-mortem characterization, compared to in situ characterization, include the ability to apply a wide range of testing conditions (including very-high-cycle fatigue), the ability to test samples with large dimensions and meaningful ranges of microstructures and the ability to characterize multiple samples. Prior work has primarily focused on characterizing one-off test specimens. In this study, the results from the nf-HEDM and X-ray CT measurements of six different specimens were used to analyze the crystallographic nature of short-crack path selection in the material and to correlate the short-crack paths to a wide range of local microstructural features, in particular the three-dimensional character of grain boundaries and the orientations of leading and trailing grains across the full CF.

2 | MATERIALS AND METHODS

2.1 | Materials

Mg alloy WE43 was provided by Magnesium Elektron Ltd. The alloy has a nominal composition in weight % of 3.74 Y, 2.10 Nd, 0.52 Gd, 0.45 Zr, 0.016 Zn, and balance Mg. The material was hot rolled to 26 mm and aged in the T5 condition (48 h at 204°C). The as-received plate was solution heat treated at 525°C for 8 h and aged at 250°C for 4 h, referred to as the underaged (UA) condition, resulting in an average grain size of 115 ± 52 μm, as shown in Figure 1A,B. The WE43-UA material displays a weak (maximum multiples of random distribution [MRD] of approximately 2.7) strength rolled basal texture as displayed in the pole figures in Figure 1C, with the center of the pole figures aligned parallel to the rolling axis. The UA heat treatment results in a fine distribution of β' precipitates in the matrix, coarse plate-like β_1 and β_1/β precipitates aligned parallel to prismatic planes in the matrix, and stringers of globular precipitates along grain boundaries as shown in Figure 2.[26,27] The tensile yield strength, ultimate tensile strength, and fatigue strength at 10^9 cycles are 139, 235, and 65 MPa, respectively, as characterized by Githens28 and Adams et al.[27]

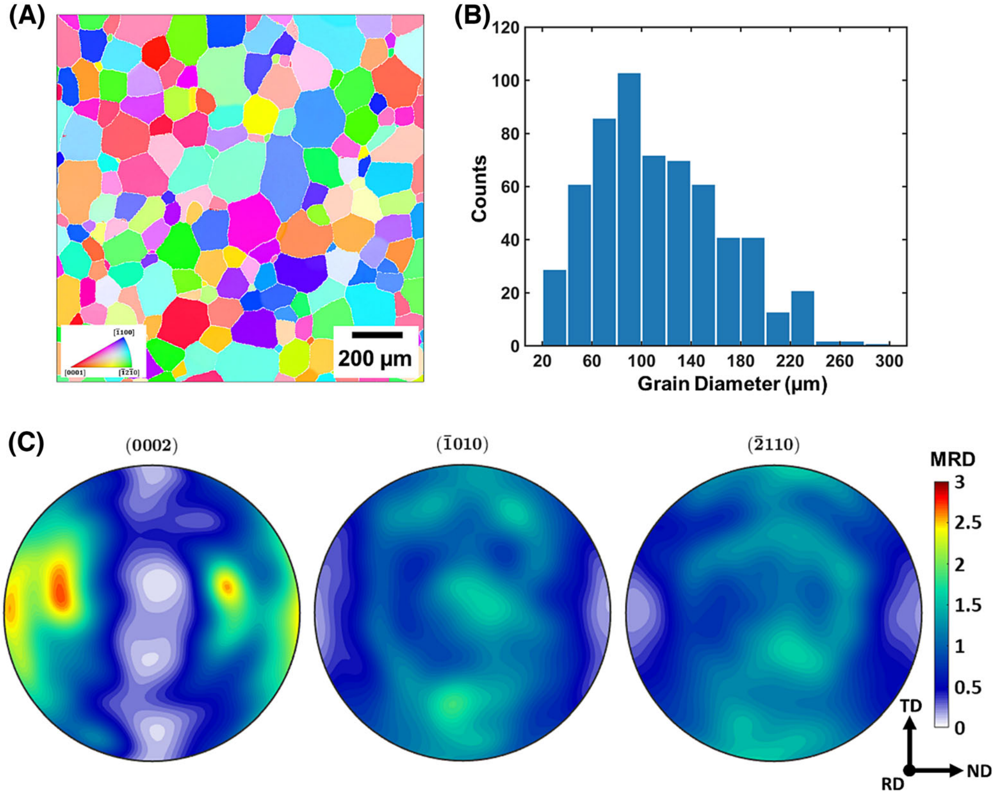

FIGURE 1 (A) The WE43-UA grain structure reconstructed using electron backscatter diffraction. Grain color is assigned using the HCP inverse pole figure (IPF) key with respect to the rolling direction Y^L. (B) Grain size distribution following the solution heat treatment and UA heat treatment in WE43. (C) Pole figures depicting the initial microstructure texture. The rolling and fatigue loading axis is out-of-plane, the horizontal poles are aligned with the normal direction, and the vertical poles are aligned with the transverse direction. [Colour figure can be viewed at wileyonlinelibrary.com]

2.2 | Mechanical testing

Fatigue specimens were tested in cylindrical and foil geometries. The foil geometry was selected to analyze crack growth across a thin microstructure on the order of the grain size of the material, and the cylindrical geometry was selected to analyze conventional radial fatigue crack growth with the CF concurrently sampling multiple grains. The cylindrical specimens were machined with a gauge diameter of 4 mm and a gauge length of 7.5 mm as shown in Figure 3B, with the tensile axis aligned with the rolling direction of the plate. Diametrically opposed flats were machined along the gauge length. The gauge flats were hand polished using a 1-μm diamond suspension and electropolished in 3:5 85% phosphoric acid to 95% ethanol for 30 min. Dogbone foil specimens were electrical discharge machined to a specimen length of 30.5 mm, gauge length of 1.6 mm, gauge width of 2 mm, and foil thickness of 300 μm as shown in Figure 3C. The foils were hand polished to an approximate thickness of 200 μm and electropolished to a thickness of 150 μm in 3:5 85% phosphoric acid to 95% ethanol, as detailed by Adams.[29] For controlled crack initiation, 100 μm × 6 μm × 50 μm focused ion beam (FIB) notches were machined in large grains with high basal nominal SFs, along the gauge flats of two cylindrical specimens and along the gauge edge of four foil specimens. The FIB notches were aligned parallel to the basal plane in cylindrical specimen 1 and perpendicular to the loading axis in the foil specimens and cylindrical specimen 2.

Very-high-cycle fatigue short-crack growth tests were performed using ultrasonic fatigue,[30–32] and the ultrasonic fixture setup is detailed in Figure 3A.[27,30] Ultrasonic fatigue testing was performed at a frequency of 20 kHz and a stress amplitude of 85 MPa in ambient air for the cylindrical samples and 60 MPa in ambient air for the foil samples. Cylindrical specimen cycling was performed at $R = -1$, and foil cycling was performed at $R = 0.1$ to avoid buckling in the thin cross section. Cycling was performed with a 200/9000 ms pulse/pause duty cycle to avoid excessive sample heating. The surface crack-growth rates were measured on the cylindrical samples using ultrasonic fatigue scanning electron microscopy and on the foil samples using optical microscopy.

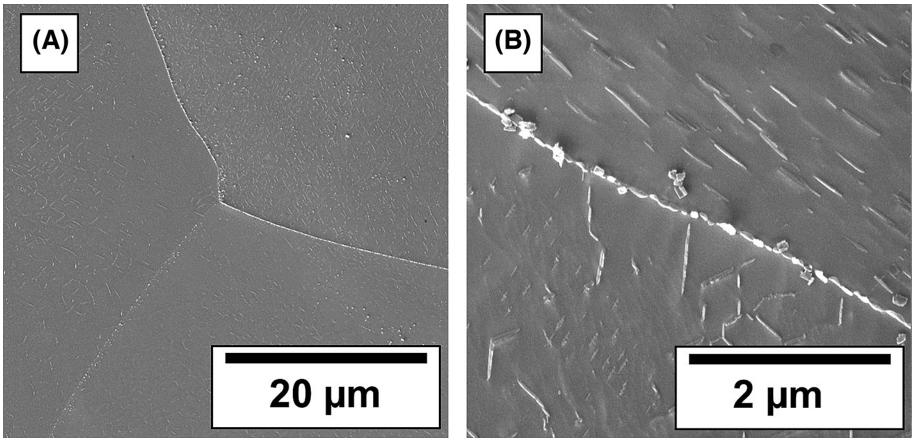

FIGURE 2 Scanning electron micrographs of the precipitate structure in WE43 following solution heat treatment at 525°C for 8 h and underaged (UA) heat treatment at 250°C for 4 h, adapted from Ganesan et al.[26] The matrix contains a fine distribution of β' precipitates, coarse plate-like β_1 and β_1/β precipitates aligned parallel to prismatic planes, and globular precipitates decorating grain boundaries.

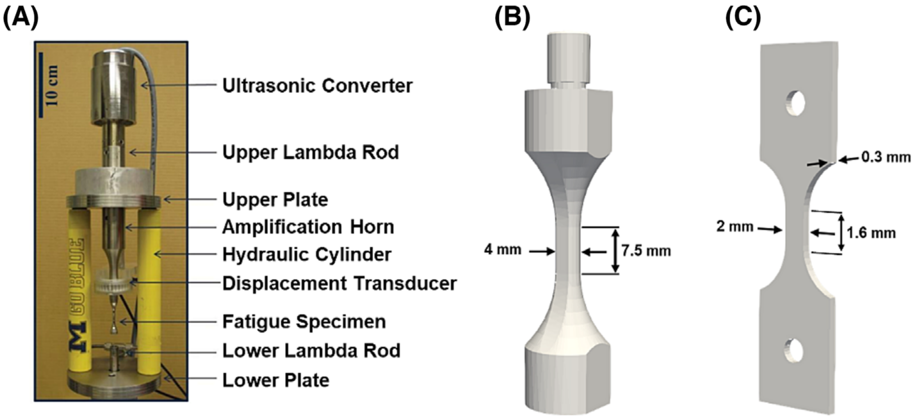

FIGURE 3 (A) Ultrasonic fatigue fixture setup, adapted from Geathers et al.,[30] (B) cylindrical test specimen geometry, and (C) thin-foil test specimen geometry. [Colour figure can be viewed at wileyonlinelibrary.com]

2.3 | Synchrotron X-ray measurements

From each portion (top and bottom) of each failed cylindrical test specimen, a matchstick-like sample with 1 × 0.5-mm cross section was extracted from the region surrounding the FIB notch using a precision low speed diamond saw. For each of the four foil test specimens, matchstick-like samples containing the first 1 mm of crack growth on the top and bottom portions of the failed specimens, starting at the FIB notch, were also extracted using a precision low speed diamond saw. The top sample from each cylindrical specimen was rotated, aligned, and affixed to the bottom sample to form 1 mm × 1 mm mounts. The top sample from foil specimen 1 was rotated, aligned, and affixed to the bottom sample to form a 1 mm × 0.3 mm mount. The top and bottom samples of foils 2–4 were aligned and combined into two mounts, one mount containing foil 2 and the top half of foil 3, and the second containing foil 4 and the bottom half of foil 3.

The mounted samples were characterized at the 1-ID beamline of the Argonne National Laboratory Advanced Photon Source using HEDM and X-ray CT. The geometry of the HEDM detector setup is detailed in Figure 4. The laboratory and detector reference frames are displayed by the axes with L and D subscripts, respectively, with the laboratory coordinate system based on the MIDAS reconstructed reference frame and the detector coordinate system based on the APS reference frame. The incoming X-ray travels along $+\widehat{e}_X^L$ and the sample is rotated around $\widehat{e}_Z^L$ by rotation angle ω. The diffracted beam is characterized by the Bragg angle 2θ and the azimuthal angle η in the $\widehat{e}_X^D$-$\widehat{e}_Y^D$ plane. X-ray CT measurements of a 1 mm × 1 mm × 800 μm volume from the top of the fracture surfaces were obtained using a PointGrey Grasshopper CMOS camera focused on a detector deploying a LuAG:Ce scintillator and a 7.5× objective with a pixel size of 0.781 μm, in a parallel beam. Images were obtained at 0.25° rotation intervals over a full rotation of 360° with an exposure of 0.2 s, and five images were taken per interval for enhanced image quality. Diffraction patterns from ff-HEDM were imaged on a GE-41RT amorphous-Si area detector with a pixel size of 200 μm, using a 1.7 mm × 100 μm box beam. Stacked 100-μm layers spanning the top of the fracture surface on each sample were imaged at intervals of 0.25° over a full rotation of 360° with an exposure of 0.2 s. Diffraction patterns from nf-HEDM were obtained with a custom detector, which is based on a QImaging Retiga 4000DC CCD camera coupled to a 5× objective focused on a LuAG:Ce scintillator, with a pixel size of 1.48 μm and a field of view of 3 mm. Measurements in the nf-HEDM geometry were performed using a line-focused beam with scan intervals of 0.25° over a 180° rotation and an exposure of 2 s. Measurements were taken at detector distances of 5 and 8 mm for each layer (Figure 4A). Cylindrical sample 1 was measured with a layer height of 11 μm, and cylindrical sample 2 was measured with a layer height of 12 μm. The foil samples were imaged with layer heights

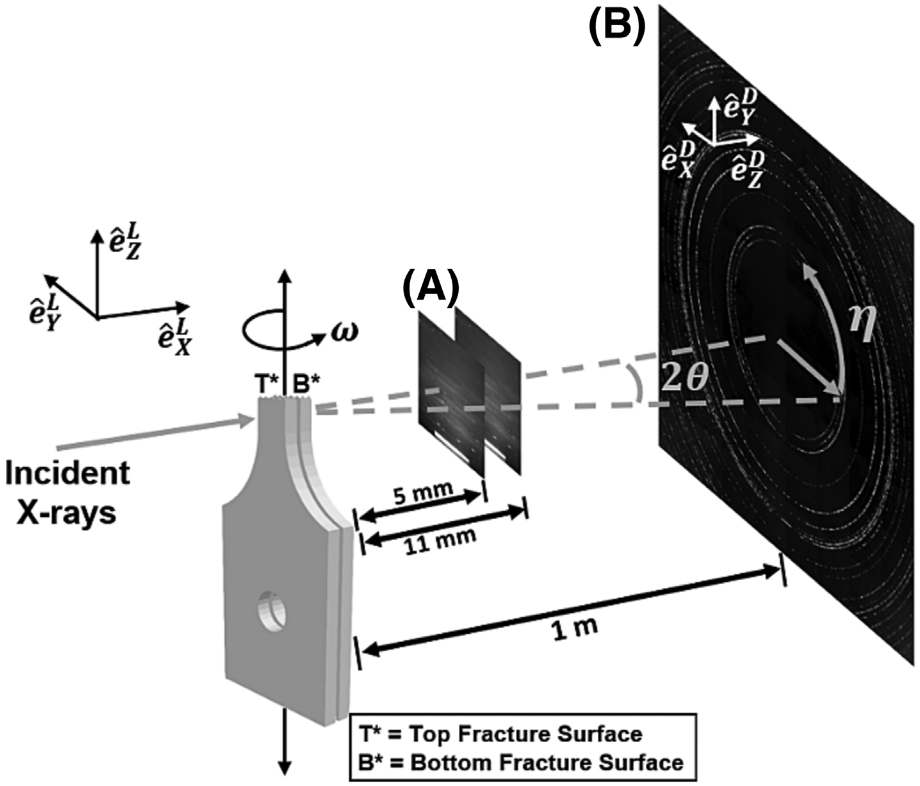

FIGURE 4 Post-mortem specimen and detector geometry for (A) nf-HEDM and (B) ff-HEDM. The coordinate system in the laboratory (MIDAS) reference frame is shown as $\left[\widehat{e}_X^L, \widehat{e}_Y^L, \widehat{e}_Z^L\right]$, and the coordinate system of the detector (APS) reference frame is shown as $\left[\widehat{e}_X^D, \widehat{e}_Y^D, \widehat{e}_Z^D\right]$. Near-field and far-field HEDM diffraction patterns are collected at sample rotation intervals ω about the loading axis $\widehat{e}_Z^L$. The diffracted beam is characterized by the Bragg angle 2θ and the azimuthal angle η in the $\widehat{e}_X^D$-$\widehat{e}_Y^D$ plane. Schematic not to scale.

varying from 11 to 15 μm. All HEDM measurements were obtained using a monochromatic beam with an X-ray beam energy of 55.618 keV. The nf-HEDM data from cylindrical sample 2 were reconstructed using the Ice-Nine software package,[33] and the nf-HEDM data from cylindrical sample 2 and the foil samples were reconstructed using the MIDAS software package.[34,35] The spatial and orientation resolutions of the near-field reconstruction are ∼2 μm and ∼0.1°, respectively. The X-ray CT volume was used to define the nf-HEDM reconstruction boundary, and the grain orientation search space was seeded by grain mean orientation data from ff-HEDM measurements. Although ff-HEDM is capable of providing mean lattice strains for each grain, the strain reconstructions were not analyzed in the current study as the focus was on crystallography.

2.4 | Quantification of short-crack path crystallography

The three-dimensional short-crack paths were reconstructed by registering the X-ray CT and nf-HEDM reconstructions for each sample. The X-ray CT reconstruction was first rotated and scaled by the detector pixel resolution to align the X-ray CT and nf-HEDM reconstructions. As the two fracture halves for any given sample were measured with the nominal fracture-surface normal oriented approximately parallel to the positive $\widehat{e}_Z^L$ direction (Figure 4), the X-ray CT reconstruction containing the top fracture surface was then manually rotated and aligned with the X-ray CT reconstruction containing the bottom fracture surface, and the resulting transformation to ensure proper alignment was recorded. Next, the voxelized nf-HEDM reconstruction containing the top fracture surface was transformed according to the transformation recorded in the previous step. Finally, the crystal orientations from the nf-HEDM reconstruction containing the top fracture surface were updated by rotating their reference frame based on the rotation determined from X-ray CT registration, as illustrated in Figures 5A and 6. Using a triangulated representation of the bottom fracture surface from the high-resolution X-ray CT reconstruction as the reference fracture surface, each triangular facet in the fracture surface was assigned the crystal orientations of the nf-HEDM voxels immediately above and below the facet. The mode of crack growth (inter- or intragranular) was identified by applying a misorientation threshold to each facet. If the misorientation between the top and bottom crystal orientations for a given facet was below the specified threshold, the crack was deemed to have propagated through a grain (intragranular), and if the misorientation exceeded the threshold, the crack was deemed to have propagated along a grain boundary (GB) coincident with the facet (intergranular). A range of threshold values was tested to accommodate error arising from slight misalignment between the two fracture halves and orientation

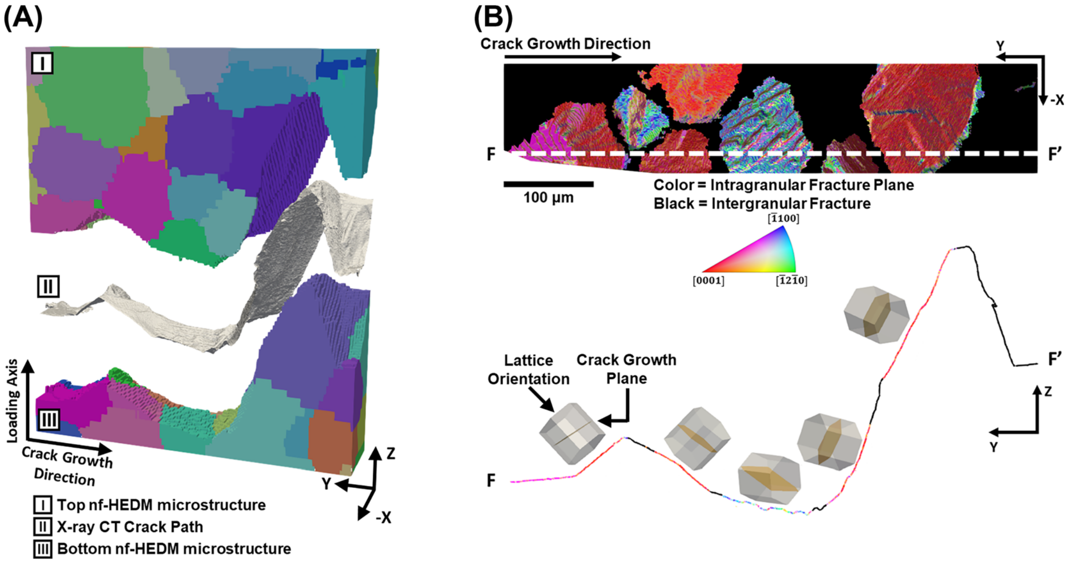

FIGURE 5 (A) Rotated and aligned top and bottom nf-HEDM three-dimensional grain structure along the fracture path in the thin-foil 1 sample, surrounding the high-resolution X-ray CT reconstructed lower fracture surface. (B) Top-down view IPF map of the fracture surface displaying the intragranular (color) and intergranular (black) regions of short-crack growth in the thin-foil 1 sample, and side-view IPF slice F-F′ of the fracture path displaying intragranular crack growth through five grains followed by intergranular crack growth. The short crack initiates at an FIB notch on the left side of the foil and propagates nominally along $-\widehat{e}_Y^L$. [Colour figure can be viewed at wileyonlinelibrary.com]

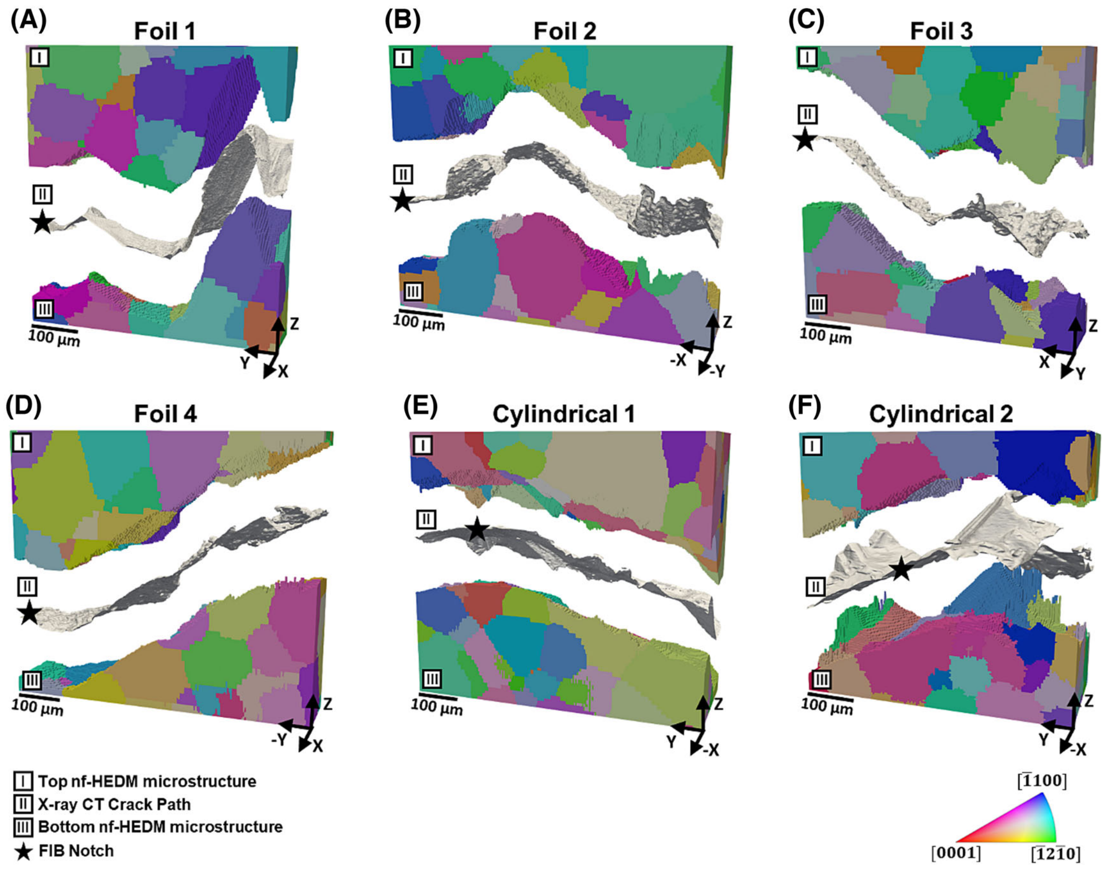

FIGURE 6 Rotated and aligned top and bottom nf-HEDM three-dimensional grain structure along the fracture path in the (A–D) thin-foil samples 1–4 and (E,F) cylindrical samples 1–2, surrounding the high-resolution X-ray CT reconstructed lower fracture surface. Voxels in the nf-HEDM reconstructions are color mapped using the HCP inverse pole figure key with respect to the loading axis ($\hat{e}_Z^L$). [Colour figure can be viewed at wileyonlinelibrary.com]

gradients within grains, and a 15° misorientation threshold was selected. To verify the reconstruction, the nf-HEDM morphologies of the top and bottom halves of a random sampling of grains that displayed intragranular crack growth were visually analyzed, and the combined shape of the top and bottom halves was confirmed to adhere to the equiaxed grain shape expected for the measured alloy condition. The crack-surface crystallography in the intragranular regions was mapped by resolving each crack-surface-facet normal into the crystallographic reference frame of the adjacent parent grain, thereby finding the lattice plane coincident with the crack-surface facet. The reconstruction procedure is detailed further by Spear et al.[21] A resulting map for one of the WE43 samples is exemplified in Figure 5B, where the intragranular regions are colored according to the IPF color map, and the black regions correspond to intergranular crack growth. The character of crack growth across each region of the fracture surface was classified as basal, non-basal, or intergranular based on the crack-surface crystallography maps. This process was repeated for each sample, and the crack-surface crystallography maps for all six test samples are displayed in Figure 7. GB traces are depicted by white curves, and the location of the FIB notch in each sample is shown with a white star. The crack propagated nominally radially away from the FIB notch in an approximate semi-circular path in each of the two cylindrical samples, and the crack propagated nominally from left to right in each of the four foil samples shown in Figure 7.

3 | RESULTS

3.1 | Short-crack growth crystallography

The crystallographic nature of short-crack path selection was analyzed by manually selecting 81[*] CF-GB

---

[*] CF-GB events where the crack front propagated along either a small—on the order of a few voxels in width—intragranular portion of a grain or a small slice of a grain boundary were removed from the analysis. Crack front intersections with small sections of grains along the outer free surfaces of the thin-foil samples or the outer edges of the cut surfaces were also removed.

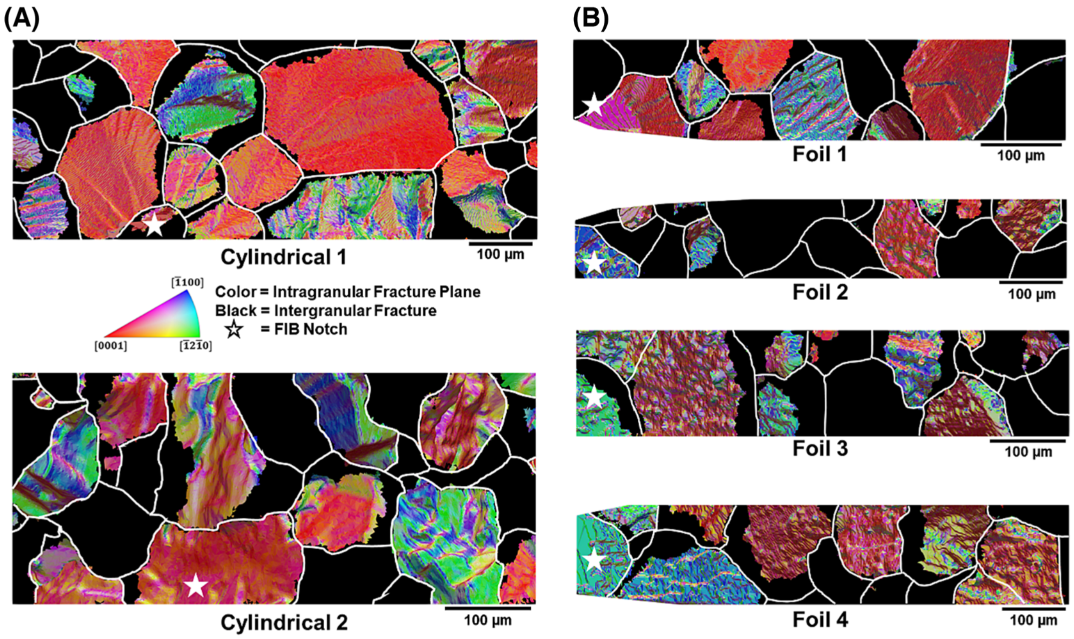

FIGURE 7 (A) Top-down view IPF map of the fracture surfaces in the two cylindrical samples displaying the intragranular (color) and intergranular (black) regions. The cracks initiated at FIB notches located at the white star in each cylindrical sample and propagated radially outwards. (B) Top-down view IPF map of the fracture surfaces in the four thin-foil samples. The cracks initiated at FIB notches on the left side of the foils located at the white stars and propagated from left-to-right. [Colour figure can be viewed at wileyonlinelibrary.com]

intersection events from the six measured specimens. The CF in the foil samples was assumed to propagate left-to-right with a CF perpendicular to the foil free surface, and the CF in the cylindrical samples was assumed to propagate radially outward from the FIB notch. The CF-GB events in each sample were aggregated for the analysis as each of the six samples displayed nominally similar crack growth behavior. For a given CF-GB event, the grain that the crack previously propagated through is referred to as the trailing grain, and the grain that the crack subsequently grew into is referred to as the leading grain. In CF-GB events where the crack transitioned from intergranular to intragranular, the grain on the lower surface prior to the GB-to-intragranular crack transition is considered the trailing grain. In CF-GB events where the crack transitioned from intragranular to intergranular, the grain in front of the nominal planar path of the advancing CF when it switched to growth along the GB is considered the leading grain. Depending on the deflection of the crack path following transition to the GB, this grain may be on the top or bottom half of the sample. The full three-dimensional GB character for each CF-GB event was determined by approximating the uncracked three-dimensional microstructure using a procedure developed by Phung et al.[36] and calculating the best-fitting plane through the uncracked voxels along the boundary between each grain pair. This three-dimensional reconstruction provides insight into the subsurface boundary character that cannot be determined from traditional surface orientation analysis such as EBSD. Crack growth was intragranular in the leading grain in 62 of the measured CF-GB events, and the crack switched from intragranular to intergranular in 19 of the measured CF-GB events. Intragranular crack growth occurred primarily along a basal plane in the leading grain in 35 events, primarily along non-basal planes in the leading grain in 23 events, and primarily along a combination of both basal and non-basal planes in the leading grain in 4 events. The leading and trailing crack path crystallography for all analyzed events is summarized in Table 1.

The texture of each intragranular crack fact was determined by calculating a kernel density function of the lattice orientations normal to each X-ray CT facet in each cracked grain using MTEX.[37] The intragranular character varied notably from grain-to-grain in each of the samples, and an example of crack propagation nominally perpendicular to $\{\bar{1}2\bar{1}0\}$ (Grain A, green), $\{\bar{1}100\}$ (Grain B, blue), and $\{0001\}$ (Grain C, red) planes in foil sample 4 is shown in Figure 8A. Crack growth is observed to be non-uniform; crack growth in the nominally $\{\bar{1}2\bar{1}0\}$ Grain A also occurred partially along $\{\bar{1}100\}$ planes; and crack growth in the nominally $\{\bar{1}100\}$ Grain B also occurred partially along $\{0001\}$ planes. The texture of crack growth in the nominally $\{0001\}$ Grain C displays the highest maximum MRD of

TABLE 1 Trailing and leading crack path crystallography for all 81 analyzed CF-GB events among six WE43 specimens characterized using nf-HEDM.

Trailing crack path	Leading crack path	Number of analyzed CF-GB events
Basal intragranular	Basal intragranular	12
Basal intragranular	Non-basal intragranular	14
Basal intragranular	Basal and non-basal intragranular	2
Basal intragranular	Intergranular	8
Non-basal intragranular	Basal intragranular	16
Non-basal intragranular	Non-basal intragranular	6
Non-basal intragranular	Basal and non-basal intragranular	1
Non-basal intragranular	Intergranular	11
Intergranular	Basal intragranular	7
Intergranular	Non-basal intragranular	3
Intergranular	Basal and non-basal intragranular	1

the three grains at approximately 4.1. The cumulative texture of all intragranular regions among all six samples, weighted by facet area to account for minor variations in the tomographic reconstructions, is shown in Figure 8B. The cumulative texture displays a predominately strong $\{0001\}$ peak with a maximum MRD of 4.9, a spread of weaker texture of around 0.6–0.75 MRD along the lattice planes rotating from $\{\bar{1}100\}$ to $\{\bar{1}2\bar{1}0\}$, and a weak texture around the pyramidal $\{10\bar{1}1\}$ and $\{11\bar{2}2\}$ planes.

3.2 | Intragranular crack growth tortuosity

The grains with intragranular crack growth nominally along basal planes were visually observed to display smoother planar crack growth compared to intragranular crack growth with non-basal or mixed-mode character. This is shown in Figure 9A for cylindrical sample 1, where the intragranular facets in the top image are color mapped with respect to the lattice plane normal perpendicular to each facet while the bottom image is color mapped with respect to the angle between the X-ray CT facet normal and the loading axis (θ_Z). The red grains (in Figure 9A), indicating crack growth along a nominally basal plane, display a smaller deviation in θ_Z (in Figure 9B) across the grain compared to the non-basal intragranular grains. This was quantified by analyzing both the intragranular texture strength and the tortuosity of crack growth. Tortuosity was characterized with two metrics: the distribution of the angular deviation between each X-ray CT facet normal and the normal of the best fit plane to all facets for the crack path in a single grain (the tortuosity angle) and the distribution of the smallest Euclidean distance between each X-ray CT facet centroid and the best-fit plane to all facets in a single grain (the tortuosity distance). The cumulative distribution of the maximum MRD, mean tortuosity angle, and mean tortuosity distance for leading grains with intragranular crack growth along a basal facet (blue circle) and non-basal facet (orange triangle) in each of the six samples are displayed in Figure 9C–F. Basal crack growth displays a higher texture strength and lower tortuosity compared to non-basal crack growth, but a large distribution of texture strength and tortuosity is observed in both groups as seen in Figure 9C.

3.3 | Impact of microstructure on short-crack path selection

3.3.1 | Analysis of individual crystallographic and geometric parameters

The crack growth crystallographic character in the 81 analyzed CF-GB events was compared to various microstructural parameters to identify the influence of local microstructure on short-crack growth in Mg alloy WE43. CF-GB events were segmented according to basal, non-basal, or intergranular crack growth behavior in the leading grain, and the cumulative distributions of 16 salient microstructural parameters for each of the three categories are shown in Figure 10. Three cumulative distributions are included on each plot: CF-GB events where the leading crack growth is basal intragranular (blue circle), events where the leading crack growth is non-basal intragranular (orange triangle), and events where the leading crack growth is intergranular (green diamonds). A cumulative distribution value at a given coordinate indicates the fraction (Y) of CF-GB events in the category that are at or below a certain crystallographic parameter value (X). Cumulative distribution plots for the basal, prismatic, pyramidal I <a>, and

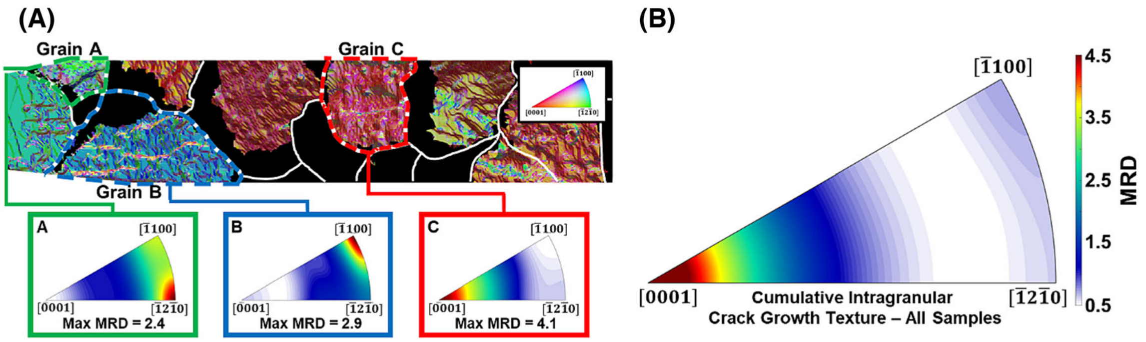

FIGURE 8 (A) Top-down IPF map of the fracture surface of the thin-foil sample 4, with the intragranular texture of two non-basal (Grain A, Grain B) and one basal (grain C) facets displayed in the inverse pole figures below. (B) Inverse pole figure displaying the cumulative intragranular texture summed across all six samples weighted by the area of each orientation-mapped X-ray CT facet. The maximum texture peak occurs at $\{0001\}$ with minor peaks at $\{\bar{1}100\}$ and $\{\bar{1}2\bar{1}0\}$. [Colour figure can be viewed at wileyonlinelibrary.com]

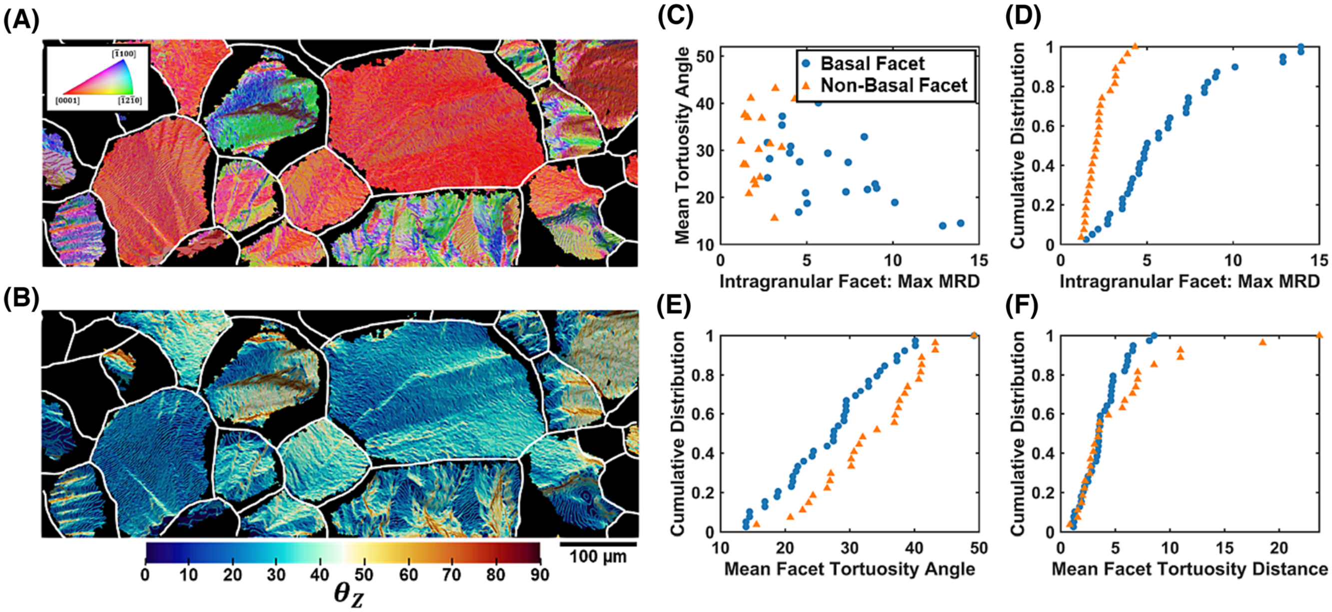

FIGURE 9 (A,B) Quantitative analysis of intragranular crack-growth regions of the cylindrical sample 1 (black corresponds to intergranular crack growth): (A) top-down IPF map of the fracture surface and (B) map of the θ_Z angular deviation between intragranular facet normals and the fatigue loading axis (out of plane). (C) Scatter plot of intragranular mean facet tortuosity angle and intragranular maximum MRD in leading grains for all analyzed CF-GB events. (D–F) Cumulative distribution plots of the intragranular maximum MRD, intragranular mean facet tortuosity angle, and mean facet tortuosity distance in the leading grains for all analyzed CF-GB events. [Colour figure can be viewed at wileyonlinelibrary.com]

pyramidal II <c+a> slip mode SFs for the leading grains are displayed in Figure 10A–D. The SFs for each slip system were calculated with respect to the nominal loading axis $\widehat{e}_Z^L$, and the maximum SF for each slip mode in each leading grain was calculated. For leading grains with a high basal SF (SF_B) of over 0.4, basal intragranular crack growth was observed in 87% of grains, non-basal intragranular crack growth was observed in 26% of grains, and the crack switched to leading intergranular crack growth at 42% of events. The prismatic SF (SF_P) (Figure 10B) cumulative distribution displays opposite behavior, with leading non-basal intragranular and leading intergranular events occurring more commonly at higher prismatic SF compared to leading basal intragranular. Out of 34 total events with leading SF_B greater than 0.4, 12% display basal intragranular crack growth, 56% display non-basal intragranular crack growth, and 32% display intergranular crack growth. Similar behavior is also observed with pyramidal I <a> SF (SF_{PA}) and pyramidal II <c+a> SF (SF_{PAC}); however, the difference in cumulative distributions is smaller. Cumulative distribution plots of the Luster–Morris geometric compatibility factor

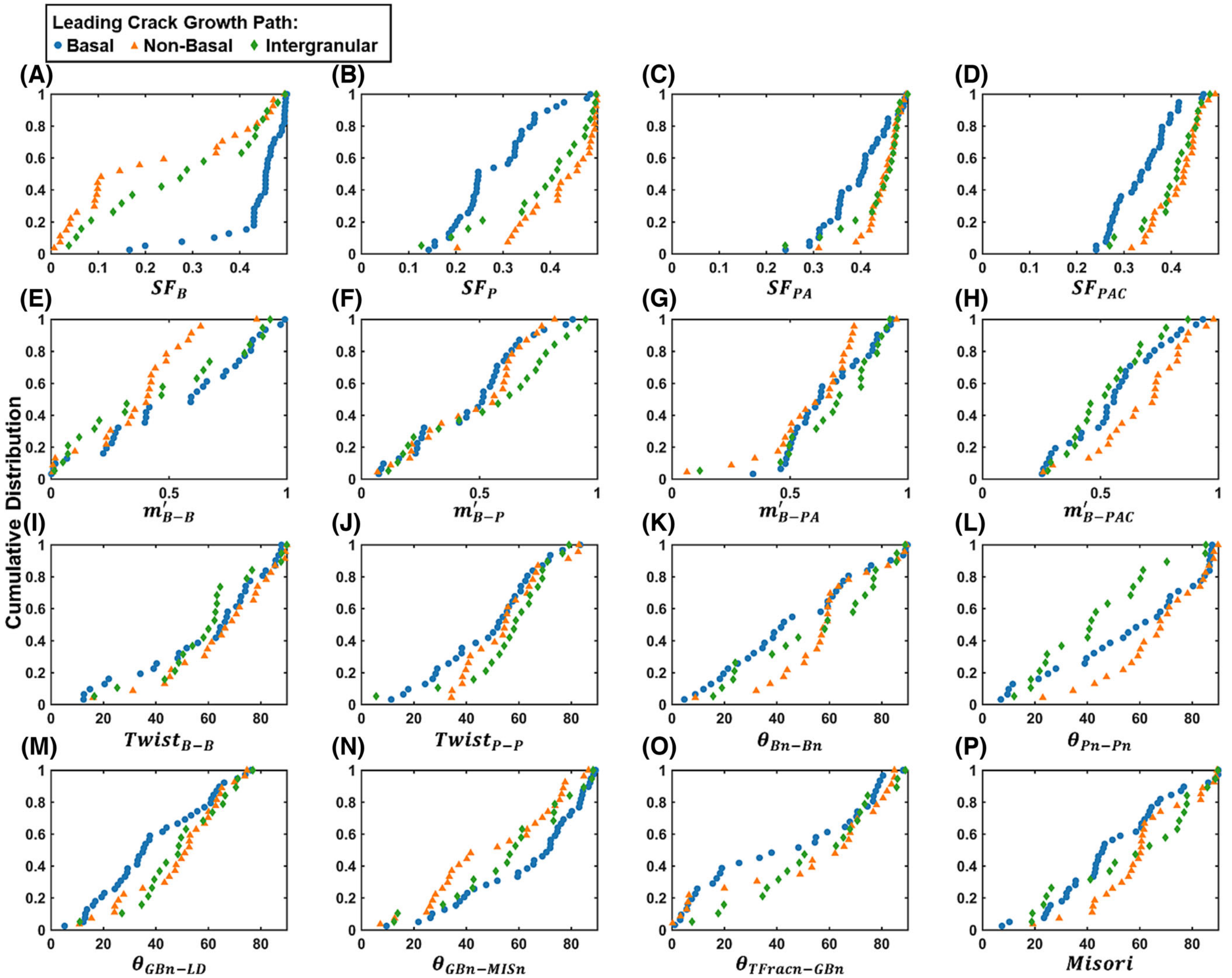

FIGURE 10 Cumulative distribution plots for crack growth in leading grains among 81 analyzed CF-GB events in six WE 43 specimens, categorized by basal, non-basal, and intergranular crack facets: (A–D) basal, prismatic, pyramidal I <a>, and pyramidal II <c+a> nominal Schmid factor in the leading grain; (E–H) trailing basal to leading basal, prismatic, pyramidal I <a>, and pyramidal II <c+a> m'; (I,J) basal to basal and prismatic to prismatic twist angle; (K) angle between trailing and leading basal plane normals; (L) angle between trailing and leading prismatic slip plane normals; (M) angle between grain boundary plane normal and loading axis; (N) angle between grain boundary plane normal and misorientation axis between trailing and leading grains; (O) angle between trailing fracture surface normal and grain boundary plane normal; (P) misorientation between trailing and leading grains. [Colour figure can be viewed at wileyonlinelibrary.com]

(m')[38] of the basal slip system in the trailing grain with each of the four slip modes in the leading grain are presented in Figure 10E–H, for each CF-GB event with intragranular crack growth in the trailing grain. The value selected for each CF-GB events is the maximum m' between the maximum SF basal slip system in the trailing grain and any slip systems in each slip mode in the leading grain. The trailing basal slip mode was used in each of the four metrics as basal slip has the lowest CRSS in WE43,[26] and it is assumed that a high percentage of basal dislocations is emitted ahead of the advancing crack tip in the trailing grain regardless of the primary plane of crack propagation. The basal-to-basal m' (m'_{B-B}) and basal-to-prismatic m' (m'_{B-P}) display slightly similar behavior, with a smaller difference in cumulative distributions, compared to SF_B and SF_P. The basal-to-pyramidal I <a> m' (m'_{B-PA}) displays negligible influence on basal versus non-basal crack path selection in the leading grain, but a larger fraction of non-basal intragranular crack growth events are observed at higher basal-to-pyramidal II <c+a> m' (m'_{B-PAC}) compared to leading basal intragranular or leading intergranular. The tilt and twist angles for every combination of slip systems with trailing intragranular were also analyzed and were observed to have minimal influence on the crack path, and the basal-to-basal twist ($Twist_{B-B}$) and prism-to-prism twist ($Twist_{P-P}$) angles are shown as examples in Figure 10I,J. The angles between slip plane normals for basal and prismatic slip systems with maximum SF in the trailing and leading grains were also analyzed. These values are related to m' but are independent of the slip direction and are presented in Figure 10K,L. Similarly, the angles between the GB plane normal and the loading axis (θ_{GBn-LD}), the misorientation axis ($\theta_{GBn-MISn}$), and the average trailing fracture facet ($\theta_{TFracn-GBn}$) are observed to impact the cumulative distribution of each crack growth category, but the exact influence of each parameter is difficult to ascertain individually. Other parameters measured with a more limited difference between cumulative distributions for different crack growth modes included the angle between the GB plane normal and the slip system normals in each leading grain, the angles between the trailing fracture plane and the leading slip planes, the angles between the loading axis and the leading slip plane normals, and the lattice plane bisected by the GB in the leading and trailing grains.

The correlation of the 24 analyzed crystallographic and geometric parameters to crack path character across all CF-GB events was further analyzed by calculating the Pearson linear correlation coefficient between each parameter and a binary classification of each CF-GB event for each of the three crack path categories (basal intragranular, non-basal intragranular, and intergranular) as illustrated in Figure 11A–C. Each linear correlation was defined as negligible ($r < 0.05$), very weak ($r < 0.2$), weak ($0.2 \leq r < 0.4$), moderate ($0.4 \leq r < 0.6$), or strong ($r \geq 0.6$). The linear correlation for all CF-GB events is illustrated in Figure 11A; the correlation for CF-GB events with intragranular leading crack growth is shown in Figure 11B; and the correlation for all CF-GB events with non-basal leading crack growth is shown in Figure 11C. For all CF-GB events, the SFs for each slip system, θ_{Bn-LD} and $\theta_{TFracn-Bn}$, generally display the highest linear correlation to the character of intragranular crack growth. The m' and twist parameters generally display very weak correlation to either intragranular character or intergranular crack growth, and m'_{B-B} and m'_{B-PAC} display weak correlation to intragranular character. Two parameters, θ_{Pn-Pn} and $\theta_{TFracn-PAn}$, correlate weakly to intergranular crack growth with very weak or negligible correlation observed to all other parameters.

3.3.2 | Basal versus non-basal intragranular crack growth

Analysis of individual crystallographic parameters proved insufficient to fully elucidate the crack path crystallographic behavior due to the complexity in the physical phenomena driving crack growth and the complex and multi-modal crack path behavior observed in WE43. Building on the individual metrics, analysis of combinations of crystallographic parameters was performed. For CF-GB events with intragranular crack growth in the leading grain, the ratio between the basal SF and

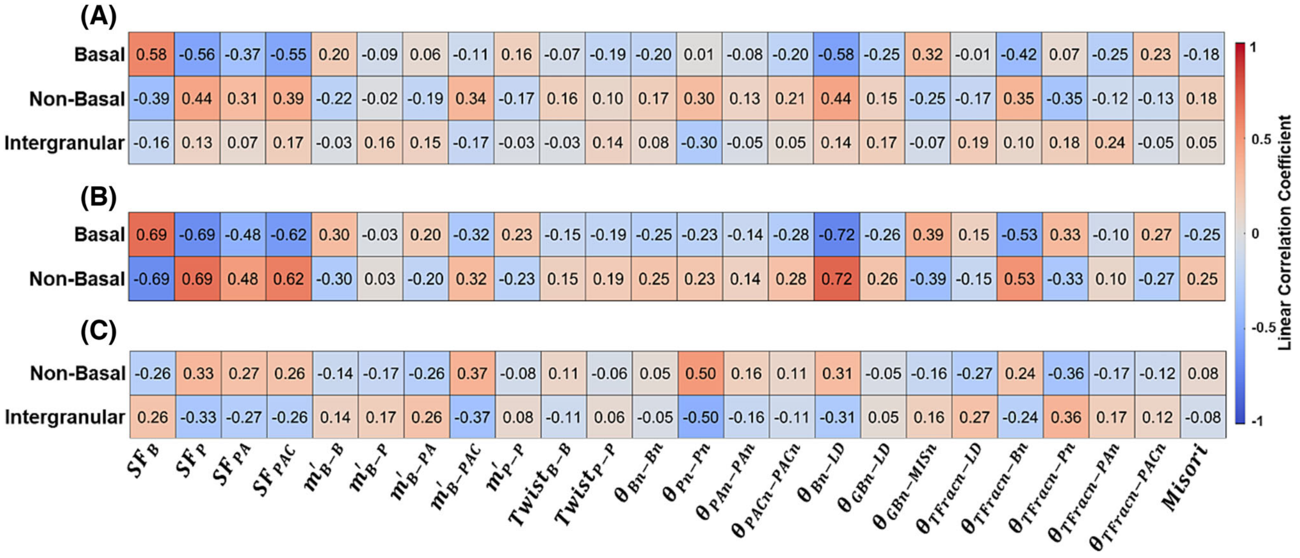

		SF_B	SF_P	SF_{PA}	SF_{PAC}	m'_{B-B}	m'_{B-P}	m'_{B-PA}	m'_{B-PAC}	m'_{P-P}	$Twist_{B-B}$	$Twist_{P-P}$	θ_{Bn-Bn}	θ_{Pn-Pn}	$\theta_{PAn-PAn}$	$\theta_{PACn-PACn}$	θ_{Bn-LD}	θ_{GBn-LD}	$\theta_{GBn-MISn}$	$\theta_{TFracn-LD}$	$\theta_{TFracn-Bn}$	$\theta_{TFracn-Pn}$	$\theta_{TFracn-PAn}$	$\theta_{TFracn-PACn}$	Misori
(A)	Basal	0.58	-0.56	-0.37	-0.55	0.20	-0.09	0.06	-0.11	0.16	-0.07	-0.19	-0.20	0.01	-0.08	-0.20	-0.58	-0.25	0.32	-0.01	-0.42	0.07	-0.25	0.23	-0.18
	Non-Basal	-0.39	0.44	0.31	0.39	-0.22	-0.02	-0.19	0.34	-0.17	0.16	0.10	0.17	0.30	0.13	0.21	0.44	0.15	-0.25	-0.17	0.35	-0.35	-0.12	-0.13	0.18
	Intergranular	-0.16	0.13	0.07	0.17	-0.03	0.16	0.15	-0.17	-0.03	-0.03	0.14	0.08	-0.30	-0.05	0.05	0.14	0.17	-0.07	0.19	0.10	0.18	0.24	-0.05	0.05
(B)	Basal	0.69	-0.69	-0.48	-0.62	0.30	-0.03	0.20	-0.32	0.23	-0.15	-0.19	-0.25	-0.23	-0.14	-0.28	-0.72	-0.26	0.39	0.15	-0.53	0.33	-0.10	0.27	-0.25
	Non-Basal	-0.69	0.69	0.48	0.62	-0.30	0.03	-0.20	0.32	-0.23	0.15	0.19	0.25	0.23	0.14	0.28	0.72	0.26	-0.39	-0.15	0.53	-0.33	0.10	-0.27	0.25
(C)	Non-Basal	-0.26	0.33	0.27	0.26	-0.14	-0.17	-0.26	0.37	-0.08	0.11	-0.06	0.05	0.50	0.16	0.11	0.31	-0.05	-0.16	-0.27	0.24	-0.36	-0.17	-0.12	0.08
	Intergranular	0.26	-0.33	-0.27	-0.26	0.14	0.17	0.26	-0.37	0.08	-0.11	0.06	-0.05	-0.50	-0.16	-0.11	-0.31	0.05	0.16	0.27	-0.24	0.36	0.17	0.12	-0.08

FIGURE 11 Single-parameter linear correlation of all 24 analyzed crystallographic and geometric parameters to (A) basal intragranular, non-basal intragranular, or intergranular crack growth for all CF-GB events; (B) basal or non-basal intragranular crack growth for CF-GB events with intragranular leading crack growth; (C) non-basal intragranular or intergranular crack growth for CF-GB events with non-basal leading crack growth. [Colour figure can be viewed at wileyonlinelibrary.com]

the maximum non-basal SF as shown in Figure 12, as well as the SF ratio weighted by the respective CRSS of the individual slip systems,[26] is observed to be a strong indicator of basal or non-basal crack growth. For leading grains with a basal SF of over 0.4 and intragranular crack growth, basal or multi-modal basal and non-basal crack growth was the dominant mechanism in 30 of 33 events. Similarly, in cases where the leading basal SF was less than 0.25 and the maximum non-basal SF was greater than 0.4, non-basal crack growth was observed in 16 of 18 events. In events where a moderate to high basal SF (e.g., greater than 0.34) and a high maximum non-basal SF (e.g., greater than 0.47) are simultaneously observed in the leading grain, the mechanism of intragranular crack growth was more stochastic with non-basal crack growth in 5 of 8 events and basal crack growth in the remaining 3 of 8.

To characterize the relative influence of a range of different crystallographic parameters, a subset of 16 parameters displaying $r \geq 0.2$ to either basal or non-basal intragranular crack growth were selected for comparative analysis. The parameters were independently centered by removing their mean and scaled by their variance, and dimensionality reduction was performed by extracting the principal component (PC) basis from a subset of CF-GB events with either basal or non-basal intragranular leading crack growth using the principal component analysis (PCA) algorithm in Scikit-Learn.[39] The linear correlation of each of the three PC axes (PC1, PC2, and PC3) to either basal or non-basal crack growth was calculated and is shown in Figure 13D, and the relative weights of each of the input crystallographic and geometric features are shown in Figure 13E. PC1 displays a strong positive correlation to non-basal crack growth and a strong negative correlation to basal crack growth, PC2 displays weaker correlation of a similar sign, and PC3 shows negligible correlation to either mechanism. The first PC axis displays a higher linear correlation than any individual parameter (Figure 11B).

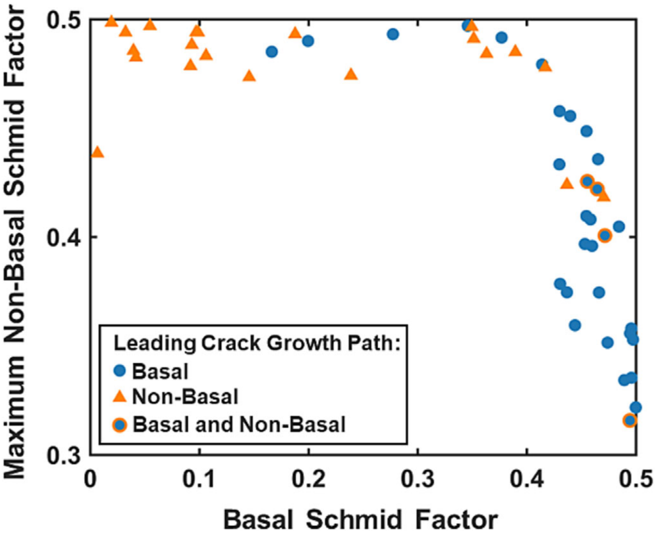

FIGURE 12 Scatter plot comparison of basal Schmid factor and the maximum non-basal Schmid factor for basal, non-basal, and combined basal and non-basal leading intragranular crack growth. [Colour figure can be viewed at wileyonlinelibrary.com]

3.3.3 | Non-basal versus intergranular crack growth

Crack growth following CF-GB events with leading grains unfavorably oriented for basal crack growth varies between non-basal intragranular crack growth and intergranular crack growth. Minor variations in linear correlation and cumulative distribution are observed for a range of different parameters, and a subset with large deviations is displayed in Figure 14. Differences in the cumulative distribution of the normal angle between the maximum SF non-basal slip systems are shown in Figure 14A–C, and the angular deviation between the trailing mean fracture plane and the maximum SF slip plane normal in the leading grain are presented in Figure 14E–G. CF-GB events with trailing intergranular crack growth or leading basal crack growth were removed for clarity. Similar to basal and non-basal intragranular character, no single parameter strongly correlates to the tendency for non-basal intragranular crack propagation or intergranular crack propagation. Two sets of binary parameter comparisons are displayed on Figure 14D,H. The advancing short crack is observed to preferentially transition to intergranular crack growths when the angle between the trailing fracture facet and the leading maximum SF prismatic slip plane normal is high (>60°), and the angle between the maximum prismatic SF slip plane normal in the trailing and leading grains is low (<60°) (Figure 14H). Intergranular crack growth is also observed to preferentially occur when the misorientation between the trailing and leading grains is high (>60°) and the GB normal is orientated approximately 45° away from the loading axis (Figure 14D).

PCA was also performed on the same subset of 16 parameters displaying $r \geq 0.2$ to either intragranular or intergranular crack growth as shown in Figure 15. The linear correlation between the individual PCs and crack path selection along non-basal intragranular versus intergranular facets is lower than that of PC1 to basal versus non-basal intragranular crack growth in Figure 13D; however, CF-GB events with high PC1, high PC2, and low PC3 correlate moderately to non-basal crack growth, and GB events with low PC1, low PC2, and high PC3

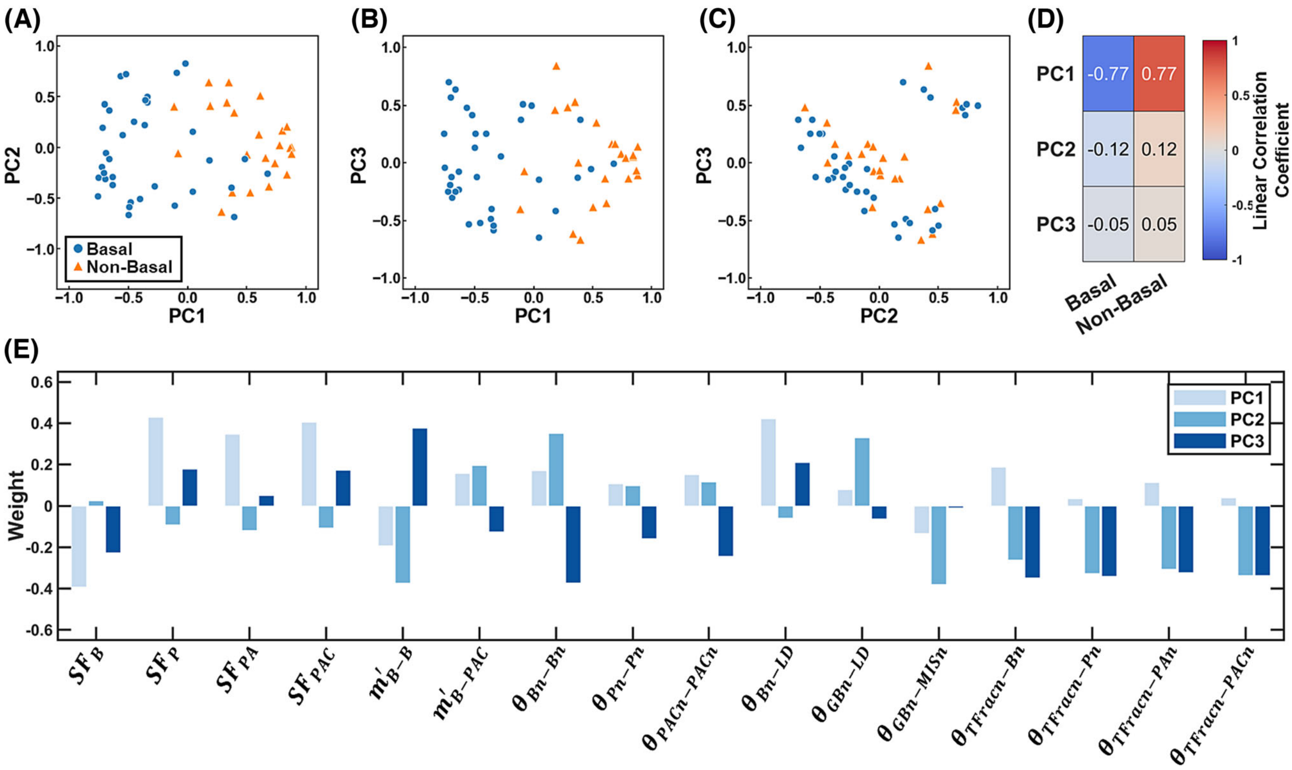

FIGURE 13 PCA for a subset of 16 of crystallographic and geometric parameters displaying $r \geq 0.2$ to either basal or non-basal intragranular crack growth for all CF-GB events with intragranular crack growth. (A–C) Scatter plots comparing the first three PCs of all CF-GB events with intragranular crack growth. Leading grains with basal crack growth are shown by the blue circle, while leading grains with non-basal crack growth are shown by the orange triangle. (D) Linear correlation coefficients for the three PCs of each CF-GB event and basal or non-basal crack growth. (E) PC basis weights for subset parameters. [Colour figure can be viewed at wileyonlinelibrary.com]

correlate moderately to intergranular crack growth. Similar to Figure 13A,B, visually prominent non-basal and intergranular clustering is observed in Figure 15A–C.

3.3.4 | Comparison of all mechanisms for leading crack growth

Analysis of the cumulative distribution of various single crystallographic and geometric parameters on basal, non-basal, or intergranular crack growth as shown in Figures 10 and 11 provided limited insight into effective metrics for classifying leading crack growth in one of the three investigated categories. Expanding on the PCA for basal versus non-basal and non-basal versus intergranular crack growth, the PC basis for the same subset of 16 parameters from all CF-GB events was calculated and correlated to all three classes of crack growth character as illustrated in Figure 16A–D. Basal intragranular crack growth correlated strongly ($r = -0.64$) to PC1, very weakly ($r = 0.16$) to PC3, and displayed negligible correlation to PC2. Non-basal intragranular crack growth correlated moderately ($r = 0.56$) to PC1, very weakly ($r = -0.19$) to PC2, and displayed negligible correlation to PC3. Intergranular crack growth displayed weak to very weak correlation ($0.13 \leq r \leq 0.2$) to each of the three PCs. Slight clustering for each of the three classes is observed in Figure 16A–C; however, noticeable overlap between classes is evident on each binary PC comparison.

The number of analyzed CF-GB events in the current study is too low to provide an in-depth comparison of classification models on crack-path prediction in WE43; however, an initial approximation was performed using the linear support vector classification (SVC) algorithm in Scikit-Learn[39] with a "l2" penalty, "hinge" loss function, and regularization parameter of 0.5. The linear SVC algorithm is a supervised machine learning model for classifying data using hyperplanes, with hyperplanes selected to separate labeled classes and maximize the distance between the margins or nearest training datapoints.[40,41] A linear kernel was chosen to limit overfitting due to the small number of samples in the input datasets. For each classification, the PC1, PC2, and PC3 datasets were split with 70% of the measured CF-GB events used to train the model, and 30% of events used to test the

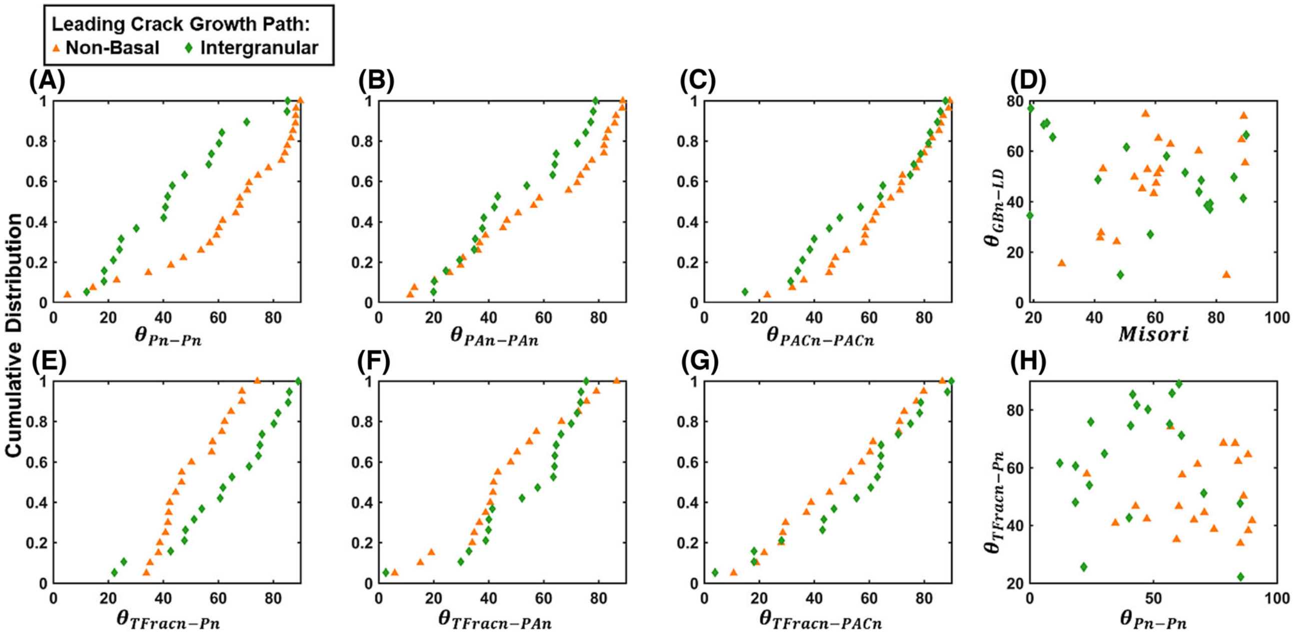

FIGURE 14 Cumulative distribution plots for leading non-basal intragranular crack growth (orange triangle) and leading intergranular crack growth (green diamond) at analyzed CF-GB events, for (A–C) angle between maximum SF prismatic, pyramidal I <a>, and pyramidal II <c+a> slip plane normals in the trailing and leading grains, (E–G) angle between trailing fracture surface normal and leading max SF prismatic, pyramidal I <a>, and pyramidal II <c+a> slip plane normals. (D) Scatter plot comparison of misorientation between trailing and leading grains and angle between GB plane normal and loading direction for CF-GB events with leading non-basal intragranular crack growth and intergranular crack growth. (H) Scatter plot comparison of angle between max SF prismatic slip plane normals in the trailing and leading grains and angle between trailing fracture surface normal and leading max SF prismatic slip plane normal for CF-GB events with leading non-basal intragranular crack growth and intergranular crack growth. [Colour figure can be viewed at wileyonlinelibrary.com]

model. The model yielded 89% accuracy in predicting basal or non-basal intragranular crack growth (Figure 13A–C), 75% accuracy in predicting non-basal intragranular or intergranular crack growth (Figure 15A–C), and 71% accuracy in predicting basal intragranular, non-basal intragranular, or intergranular crack growth (Figure 16A–C). For a comparison to the individual parameters, the linear SVC algorithm was also used to predict basal intragranular, non-basal intragranular, or intergranular crack growth from a three-parameter array consisting of the two parameters with the maximum sum correlation to all classes of crack growth (SF_B and θ_{Bn-LD}) and the parameter with the maximum correlation to intergranular crack growth (θ_{Pn-Pn}). Using a similar 70–30 test-training split, the model yielded 59% accuracy in predicting the crack path character.

4 | DISCUSSION

4.1 | Intragranular short-crack path selection in WE43

The crystallographic character of microstructurally short-crack growth in Mg alloys can vary significantly both across a single crack path and between different samples. Cracks are observed to propagate both intragranularly and intergranularly, with complicated CFs often switching back and forth between mechanisms, as observed in the six reconstructed samples in Figure 6. Intragranular crack growth occurs along basal, prismatic, and pyramidal crystallographic planes and occasionally along non-crystallographic transgranular planes, with both single-plane and multi-plane growth observed in different grains and at different distances along the CF with respect to the initial FIB notch. Intragranular path selection is influenced significantly by the orientation of grain lattices with respect to the macroscopic cyclic loading direction.

While local stress states ahead of the advancing crack tip may vary, cracks generally are observed to grow along slip planes nominally oriented favorably for dislocation slip. In WE43, the basal slip mode has the lowest CRSS, and intragranular crack growth along basal facets is observed in every characterized sample. The dominant basal intragranular crack growth, reflected in the strong {0001} MRD in the average texture across all intragranular facets, matches observations in a similar RE-strengthened Mg alloy Elektron 21.[19,42] As expected, as SF_B increases, crack growth along the basal plane is

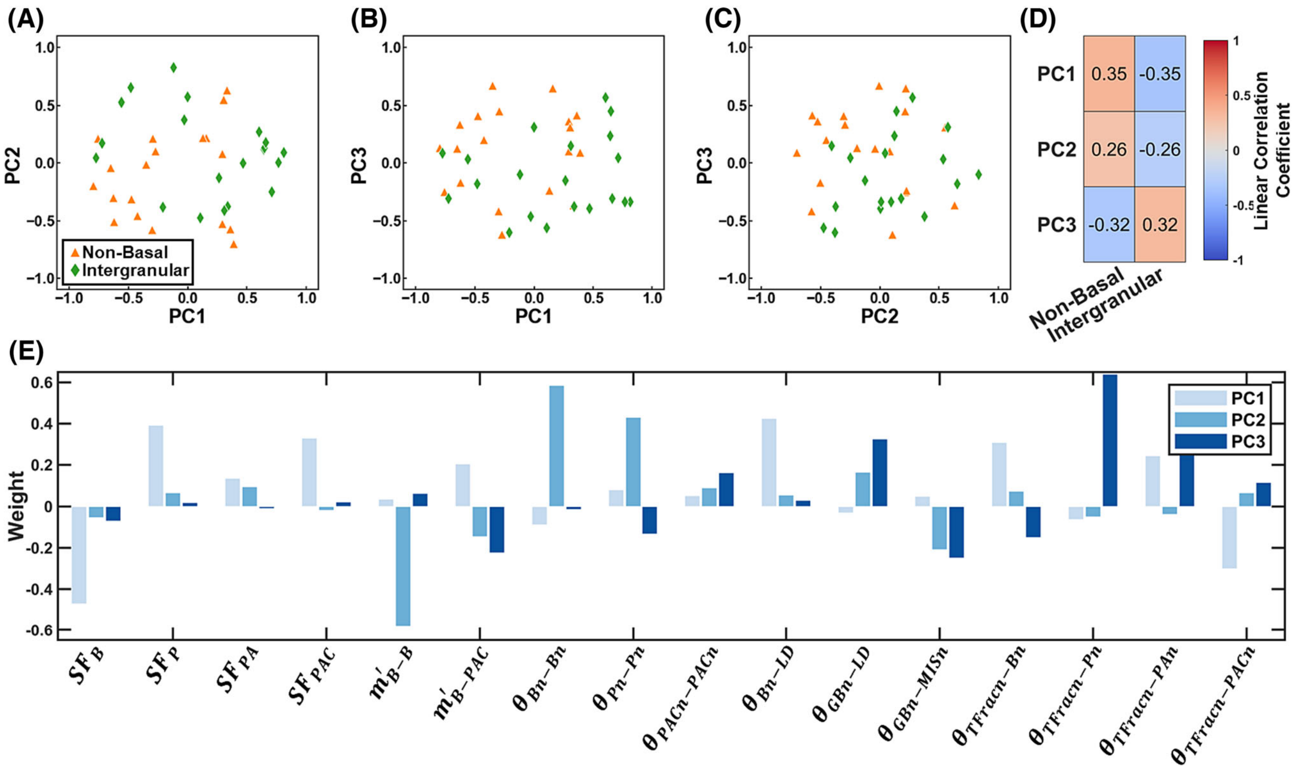

FIGURE 15 PCA for a subset of 16 of crystallographic and geometric parameters displaying $r \geq 0.2$ to either basal intragranular, non-basal intragranular, or intergranular crack growth for CF-GB events with non-basal intragranular and intergranular crack growth. (A–C) Scatter plots comparing the first three PCs of all CF-GB events without leading basal intragranular crack growth. Leading grains with non-basal crack growth are shown by the orange triangle, while leading grains with intergranular crack growth are shown by the green diamonds. (D) Linear correlation coefficients for the three PCs of each CF-GB event and non-basal or intergranular crack growth. (E) PC basis weights for subset of parameters. [Colour figure can be viewed at wileyonlinelibrary.com]

preferentially observed with over 75% of all leading grains with a basal SF of greater than 0.45 (25 of 33) displaying basal crack growth. Similarly, as the geometric compatibility between basal slip systems in the trailing and leading grain increases, basal dislocations emitted ahead of the crack tip can more easily transfer across the GB to the leading grain and provide a favorable path for crack growth. Mirroring basal SF, non-basal crack growth is preferentially observed at CF-GB events with high SF_P, SF_{PA}, and SF_{PAC} in the leading grain. Over 60% of all CF-GB events, and 89% of CF-GB events with leading intragranular growth, exhibited crack growth on non-basal planes when SF_B was less than 0.25. The specific plane of non-basal crack growth is further expected to be influenced by the ratio of the non-basal slip mode SFs to the relative non-basal slip mode CRSS in WE43; however, the small number of non-basal crack facets identified in the current study limits analysis of these parameters. Variability in intragranular crack path behavior, as observed in the high non-basal and high basal SF regions of Figure 12, may arise from heterogeneities in grain-resolved stresses deviating from the macroscopic conditions tracked by the nominal SFs. This mirrors observations in FCC alloys where the crack growth direction has been observed to preferentially follow the slip system with the highest resolved shear stress, which may vary from the slip system with the maximum nominal SF.[22] Additionally, due to the low basal to non-basal CRSS ratio in WE43, slip activity may occur on multiple seemingly unfavorable slip modes with respect to macroscopic loading conditions.

Intragranular short-crack path selection is additionally influenced by geometric factors. As the angle between the maximum SF slip plane normals in the trailing and leading grains increases, the crack will be required to deviate further (in the laboratory reference frame) across the GB to remain along the same slip mode. As an example, when the crack starts on a basal facet in the trailing grain, basal crack growth preferentially occurs in the leading grain when θ_{Bn-Bn} is low. The crack remains on a basal facet in the leading grain in 75% of events where $\theta_{Bn-Bn} < 43°$ as displayed in Figure 10K; however, the crack only remains on a basal plane in the leading grain in 15% of events where $\theta_{Bn-Bn} > 43°$. Additionally, as the geometric compatibility of any two slip systems between the trailing and leading grains

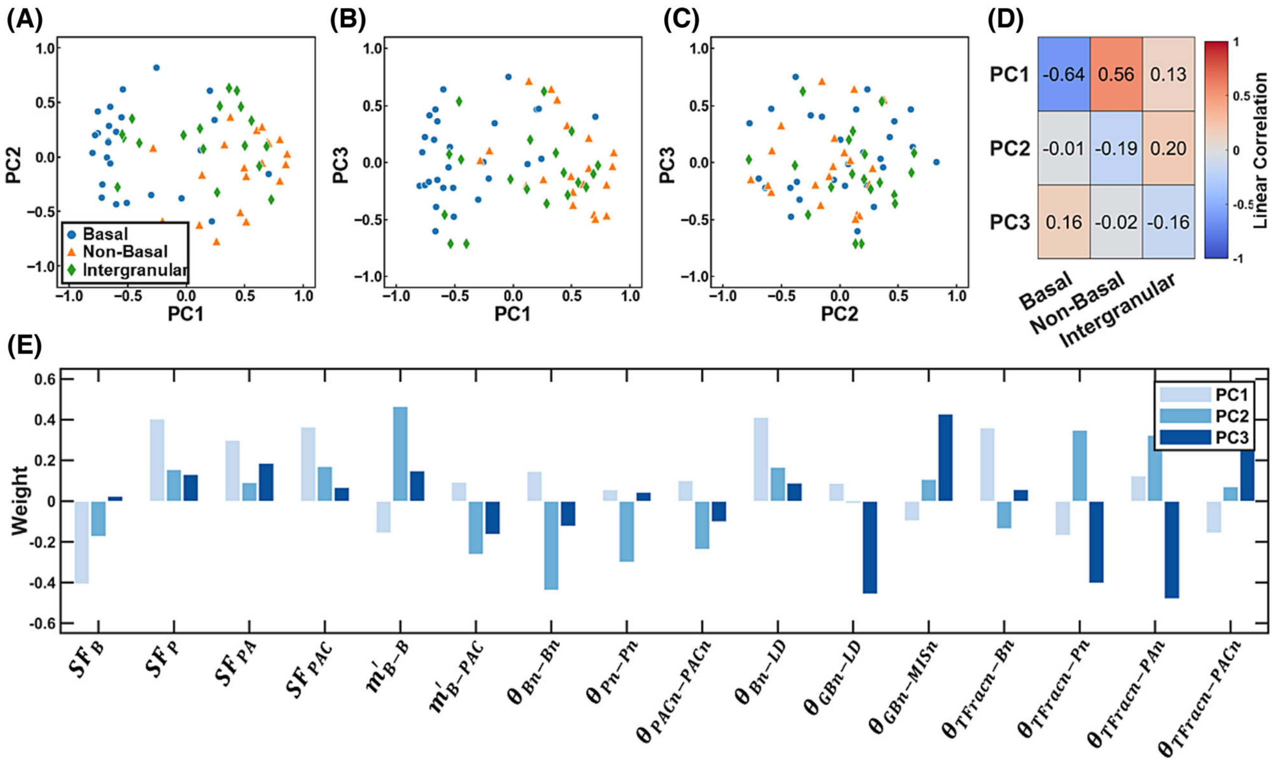

FIGURE 16 PCA for a subset of 16 of crystallographic and geometric parameters displaying $r \geq 0.2$ to either basal intragranular, non-basal intragranular, or intergranular crack growth for all CF-GB events. (A–C) Scatter plots comparing the first three PCs of all CF-GB events. Leading grains with basal crack growth are shown by the blue circles, leading grains with non-basal crack growth are shown by the orange triangle, and leading grains with intergranular crack growth are shown by the green diamonds. (D) Linear correlation coefficients for the three PCs of each CF-GB event and crack growth character. (E) PC basis weights for subset intragranular and intergranular sensitive crystallographic and geometric parameters. [Colour figure can be viewed at wileyonlinelibrary.com]

decreases, the ease of slip transfer across the GB is similarly expected to decrease. We observe a moderate impact of m'_{B-B} on crack path selection with 90% of non-basal crack growth in leading grains occurring at grain pairs with $m'_{B-B} < 0.63$; however, the geometric compatibility parameters display less of an impact than the average SF in the leading grains. This may arise in part due to the complexity of dislocation interactions at grains boundaries[43] and slip transfer in Mg alloys[44] or local heterogeneities in the stress states resolved in different grains across the CF. The misorientation angle across the GB is also observed to display a moderate impact on intragranular crack growth, matching observations of basal-to-prismatic and basal-to-pyramidal slip transfer in Mg-RE alloys at high-misorientation grain pairs.[44–46]

The twist angle, or the angular sweep along the GB plane between the two adjacent basal planes, is observed to display minimal influence on intragranular crack path selection. Tilt and twist angles at GBs have been previously observed to correlate to crack path selection and the degree of crack growth retardation prior to CF-GB intersections in Al alloys[47] and slow crack propagation in Mg alloys[19,48]; however, the exact impact of the parameters on crack path selection in Mg alloys is not well understood. In the current investigation, half of the CF-GB events with leading basal crack growth occurred between grain pairs with a $Twist_{B-B} > 66°$, and similar behavior is also observed for non-basal crack growth and non-basal twist angles. As the twist angle increases, the crack is required to fracture along an increasingly larger arc of the GB prior to transitioning into the leading grain. Crack propagation along grain boundaries occurs frequently in WE43, and this ease of GB fracture provides only a limited barrier to intragranular path selection compared to the nominal orientation of leading grains and the geometry of the advancing crack.

4.2 | Intergranular short-crack growth

In events without basal crack growth in the leading grain, crack path selection between non-basal intragranular growth and intergranular growth is more complex. In general, as the angle between the average trailing crack growth plane and the maximum SF leading prismatic, pyramidal I <a>, and pyramidal II <c+a> slip planes increases, the crack is more likely to switch to intergranular leading crack growth as shown in Figure 14E–G. This matches the geometric behavior observed with basal-to-basal crack growth compared to basal-to-non-basal crack growth. As the angular deviation required for a crack to switch to a macroscopically favored non-basal slip plane in the leading grain increases, it is expected that crack transmission to a lower angular deviation GB plane would be more favorable. Interestingly, as θ_{Pn-Pn} increases, it is more likely that the crack will grow along a non-basal plane in the leading grain as seen in Figure 14A. This is expected to be because cracks more often grow on basal planes, and a higher deviation between favored prismatic slip plane normal may lead to a lower angle between a trailing basal plane and a leading favored prismatic slip plane. As shown in Figure 14D, leading intergranular crack growth is also frequently observed in grain pairs with both $Misori > 60^{\circ}$ and θ_{GBn-LD} near 45°. In these cases, the high misorientation would provide a barrier to slip transmission across the GB, and the GB plane would be close to coincident with the macroscopic plane of maximum shear stress providing a high driving force for crack transmission along the GB plane. In similar RE-strengthened Mg alloys, slip transfer across GBs with high misorientations was only observed at grain pairs with corresponding high m' of >0.8.[45] Only a few grain pairs at the measured CF-GB events displayed high m'_{B-P}; thus, it is expected that the difficulty of dislocation transmission through the GB at high misorientations may lead to increased crack transfer to intergranular crack paths. Intergranular crack growth is also increasingly observed at low misorientation events; however, very few grain pairs were characterized with a misorientation less than 30°. The ease of slip transfer in a Mg-Y alloy was also observed to depend on both the m' between adjacent grains and the corresponding inclination of the GB plane with respect to the slip systems, or the M criterion,[46] matching the current observations of only a slight correlation with intragranular and intergranular crack growth in Figure 10M–O.

Compared to the geometry of the GB plane, the crystallographic character of the GB in the leading and trailing grain appeared to have no noticeable correlation to intragranular or intergranular crack growth in the reconstructed regions. While coincident site lattice boundaries,[49] twin boundaries,[25,50,51] and low-miller-index boundaries[25] have been previously observed to be resistant to fatigue- and corrosion-induced crack growth in a range of different alloy systems, the characterized GBs in this study were all general high angle boundaries presumably with similar values of boundary energy. Further, the grain-average orientation and GB geometry parameters do not consider local variations in the microstructure near GBs. As shown in Figure 2B, globular precipitates nucleate heterogeneously along grain boundaries in WE43 during the UA heat treatment,[29] leading to formation of precipitate free zones adjacent to boundaries. While microcracking along networks of GB precipitates has been observed in WE43 during uniaxial deformation,[52] the interaction between the advancing short-CF and GB structures is complex and may partially contribute to the stochastic nature of intragranular versus intergranular crack growth observed in the reconstructed samples. Due to length scale and contrast limitations, the 3D GB precipitate structure cannot be resolved from the X-ray CT reconstruction. Additionally, while the intersection of small twins and GBs may impact short-crack growth, no twin orientations were detected in the ff-HEDM reconstructions, and low-confidence bands, potentially indicating un-indexed twin lattices, were not detected in the nf-HEDM reconstructions.

4.3 | Crack path prediction and texture

Due to the multi-modal character of short-crack growth in WE43, accurate prediction of crack path selection at CF-GB intersections requires consideration of a wide range of crystallographic and geometric parameters, including grain average orientations, loading conditions, and the three-dimensional subsurface character of GB planes. One possible technique for integrating many competing experimentally characterized parameters into short-crack-path classification is PCA, and the linear transformation of the high-dimensional crystallographic and geometric features to a lower-dimensional space is shown to be a promising method for characterizing the combined impact of numerous CF-GB parameters intersections on subsequent crack-path selection. While an extensive comparison of dimensionality reduction and classification techniques is beyond the scope of the current work, the correlation between PCs and crack growth behavior would potentially increase with larger input datasets and number of characterized CF-GB intersections. Trained probabilistic PC classification models could be integrated into crystal plasticity fracture models[36] and graph theory models[53] to improve simulation accuracy. To aid in validating such models, the information for all 81 CF-GB events has been provided in an open dataset in the Materials Commons. Additionally, as complexities in the stress state surrounding an advancing CF can only be captured via modeling, experimentally reconstructed CF-GB parameters could be combined with numerical simulations of local mechanical states to improve the predictive accuracy of classification algorithms.

The tortuosity of the advancing CF during microstructurally short-crack growth is additionally an important consideration for part lifetime during high cycle fatigue. Highly tortuous intragranular growth increases the total crack length and surface area of a crack propagating through a grain and may impact the effective growth rate through shielding mechanisms such as surface-roughness-induced crack closure.[54,55] Predicting short-crack tortuosity is thus necessary for both accurate crack path selection and crack growth kinetics in fracture models. The tortuosity of intragranular crack growth in WE43 is observed to be linked strongly to the crystallographic nature of the crack path. Grains with intragranular crack growth across only basal facets display smooth, planar CFs with minimal crack deflection, while grains with intragranular crack growth primarily along non-basal facets often display wavy or multi-faceted CFs with the crack propagating across multiple slip planes or non-crystallographic planes simultaneously. This can be rationalized partially by the differences in CRSS between the primary slip systems in WE43. The basal to prismatic CRSS ratio varies between approximately 1:3 and 1:2 in solution heat treated (ST) and ST + T6 aged WE43, with the ratio in the characterized UA condition between the two.[26] The prismatic, pyramidal I <a>, and pyramidal II <c+a> slip modes, however, display approximately the same CRSS in the ST condition and only a slight difference in the T6 condition. Grains aligned favorably for basal slip are expected to display predominantly basal-only crack growth character, while grains with lower basal SF could activate slip on multiple non-basal modes resulting in tortuous crack propagation, as observed in multiple intragranular facets in the two cylindrical samples (see Figure 7A). Grains with low or moderate basal SF and a high non-basal SF mode may also display wavy bimodal crack growth due to mixed dislocation activity along the geometrically favored but higher CRSS non-basal plane and the lower SF but also lower CRSS basal plane. This intragranular wavy crack growth is visually evident in the center of the Foil 1 sample (Figure 7B) and the bottom left of the Cylindrical 1 sample (Figure 7A). The tendency for multi-slip plane crack growth does not appear to correlate with the distance from initial crack initiation in the imaged samples, as has been linked to a transition region from stage I to stage II crack growth previously[56]; however, it is important to note that the maximum crack path length in each sample is still on the order of only a few grain lengths. The crystallography-linked crack-path tortuosity observed in WE43 offers a possible mechanism for future microstructurally controlled short-crack growth behavior in Mg alloys using carefully tailored textures.

5 | CONCLUSIONS

The three-dimensional crystallographic character of short-crack growth in Mg alloy WE43 was characterized post-mortem using a combination of nf-HEDM and X-ray CT for six different specimens. The influence of lattice orientation, full GB character, and fracture geometry on crack growth behavior following short-crack intersection with 81 grain boundaries was classified according to primary intragranular basal, intragranular non-basal, or intergranular character. Cumulative distribution plots were generated for each classification of crack growth as a function of 24 different crystallographic and geometric parameters, and linear combinations of crystallographic parameters were correlated with crack path selection using PC analysis. The conclusions are summarized as follows:

- The crystallographic character of intragranular crack propagation in Mg alloy WE43 correlates moderately to the favorable alignment for slip activity and grain-to-grain slip transfer. Grains with high SF_B display dominant short-crack growth along basal facets, while grains with high SF_P, SF_{PA}, and SF_{PAC} preferentially display single facet, multi-modal, or non-crystallographic crack growth along non-basal planes.
- Grain-average orientation is observed to be a stronger predictor for intragranular crack path selection than slip mode geometric compatibility or tilt-twist alignment across grain boundaries.
- Intergranular crack growth occurs easily in Mg alloy WE43, with crack paths transitioning from intragranular to intergranular and vice versa across the three-dimensional crack paths. Intergranular crack growth displays a lower association to local crystallography and crack path geometry, with 50% and 49% lower mean linear correlation across the 24 analyzed parameters compared to basal intragranular and non-basal intragranular crack growth respectively.
- Moderate to strong linear correlation between PCs and short-crack path selection is observed following dimensionality reduction on a subset of 16 crystallographic and geometric parameters. The linear correlation between PC1 and basal intragranular crack growth is slightly higher than the linear correlation of individual parameters. The strength of the linear correlation between the PCs and non-basal intragranular and intergranular crack growth is similar to the linear correlation of individual parameters; however, the classification accuracy for crack path crystallography improves following PCA compared to subsets of individual high-correlation parameters.

AUTHOR CONTRIBUTIONS

Duncan Greeley: formal analysis, investigation, methodology, data curation, HEDM data reconstruction, writing—original draft. Jacob Adams: methodology, investigation, data curation, writing—review. Peter Kenesei: resources, data curation, HEDM data reconstruction, beamline support, writing—review. Ashley Spear: conceptualization, methodology, fracture surface reconstruction algorithm development, writing—review and editing. John Allison: conceptualization, project administration, supervision, writing—review and editing.

ACKNOWLEDGMENTS

This work was supported by the U.S. Department of Energy, Office of Basic Energy Sciences, Division of Materials Sciences and Engineering under Award # DE-SC0008637 as part of the Center for Predictive Integrated Structural Materials Science (PRISMS Center) at University of Michigan. This research used resources of the Advanced Photon Source, a U.S. Department of Energy (DOE) Office of Science user facility operated for the DOE Office of Science by Argonne National Laboratory under Contract No. DE-AC02-06CH11357. DG also acknowledges support from the University of Michigan Rackham Merit Fellowship Program and the University of Michigan Predoctoral Fellowship Program. ADS acknowledges support provided by the National Science Foundation under Grant No. CMMI-1629660. We also thank Dr. Dillon Watring, Quinn Johnson, and Jayden Plumb who assisted in collecting the HEDM data. We thank Dr. Brian Phung for assistance with reconstructing the uncracked microstructures from the separate nf-HEDM datasets. We thank Dr. Hemant Sharma and Dr. Jun-Sang Park of the Advanced Photon Source for assistance with MIDAS data reconstructions and Dr. Jonathan Lind and Dr. Shiu Fai Li for assistance with IceNine near-field HEDM data reconstructions. We thank Dr. Wayne Jones for design of the ultrasonic fatigue setup.

CONFLICT OF INTEREST STATEMENT

On behalf of all authors, the corresponding author states that there is no conflict of interest.

DATA AVAILABILITY STATEMENT

The data that support the findings of this study are available from the corresponding author upon reasonable request.

NOMENCLATURE

m'_{B-B}	maximum m' between basal slip systems with maximum SF in the trailing grain and leading grain
m'_{B-P}	maximum m' between basal slip system with maximum SF in the trailing grain and all prismatic slip systems in the leading grain
m'_{B-PA}	maximum m' between basal slip system with maximum SF in the trailing grain and all pyramidal I <a> slip systems in the leading grain
m'_{B-PAC}	maximum m' between basal slip system with maximum SF in the trailing grain and all pyramidal II <c+a> slip systems in the leading grain
m'_{P-P}	maximum m' between prismatic slip system with maximum SF in the trailing grain and all prismatic slip systems in the leading grain
Misori	misorientation (°) between trailing and leading grains
SF_B	maximum nominal basal Schmid factor among all slip systems in the leading grain
SF_P	maximum nominal prismatic Schmid factor among all slip systems in the leading grain
SF_{PA}	maximum nominal pyramidal I <a> Schmid factor among all slip systems in the leading grain
SF_{PAC}	maximum nominal pyramidal II <c+a> Schmid factor among all slip systems in the leading grain
$Twist_{B-B}$	twist angle (°) between trailing and leading basal slip systems
$Twist_{P-P}$	minimum twist angle (°) between all trailing and leading prismatic slip systems
θ_{Bn-Bn}	angle (°) between slip plane normals for basal slip systems with maximum SF in the trailing and leading grains
θ_{Bn-LD}	angle (°) between leading basal slip plane normal and loading direction
θ_{GBn-LD}	angle (°) between grain boundary plane normal and loading direction
$\theta_{GBn-MISn}$	angle (°) between grain boundary plane normal and misorientation axis between trailing and leading grains
θ_{Pn-Pn}	angle (°) between slip plane normals for prismatic slip systems with maximum SF in the trailing and leading grains
$\theta_{PAn-PAn}$	angle (°) between slip plane normals for pyramidal I <a> slip systems with maximum SF in the trailing and leading grains
$\theta_{PACn-PACn}$	angle (°) between slip plane normals for pyramidal II <c+a> slip systems with maximum SF in the trailing and leading grains

$\theta_{TFracn-Bn}$	angle (°) between trailing fracture surface normal and slip plane normal for basal slip system with maximum SF in the leading grain
$\theta_{TFracn-GBn}$	angle (°) between trailing fracture surface normal and grain boundary plane normal
$\theta_{TFracn-Pn}$	angle (°) between trailing fracture surface normal and slip plane normal for prismatic slip system with maximum SF in the leading grain
$\theta_{TFracn-PAn}$	angle (°) between trailing fracture surface normal and slip plane normal for pyramidal I <a> slip system with maximum SF in the leading grain
$\theta_{TFracn-PACn}$	angle (°) between trailing fracture surface normal and slip plane normal for pyramidal II <c+a> slip system with maximum SF in the leading grain

ORCID

Ashley D. Spear https://orcid.org/0000-0002-3933-3131

REFERENCES

1. Suresh S. *Fatigue of Materials*. 2nd ed. Cambridge University Press; 1998.
2. Castelluccio GM, Musinski WD, McDowell DL. Recent developments in assessing microstructure-sensitive early stage fatigue of polycrystals. *Curr Opin Solid State Mater Sci*. 2014;18(4):180-187.
3. Suresh S, Ritchie RO. Propagation of short fatigue cracks. *Int Met Rev*. 1984;29(1):445-475.
4. Partridge PG. The crystallography and deformation modes of hexagonal close-packed metals. *Metall Rev*. 1967;12(1):169-194.
5. Agnew SR, Duygulu Ö. Plastic anisotropy and the role of non-basal slip in magnesium alloy AZ31B. *Int J Plast*. 2005;21(6):1161-1193.
6. Bohlen J, Yi S, Letzig D, Kainer KU. Effect of rare earth elements on the microstructure and texture development in magnesium-manganese alloys during extrusion. *Mater Sci Eng A*. 2010;527(26):7092-7098.
7. Stanford N, Barnett MR. The origin of "rare earth" texture development in extruded mg-based alloys and its effect on tensile ductility. *Mater Sci Eng A*. 2008;496(1–2):399-408.
8. Chakkedath A, Bohlen J, Yi S, Letzig D, Chen Z, Boehlert CJ. The effect of nd on the tension and compression deformation behavior of extruded Mg-1Mn (wt pct) at temperatures between 298 K and 523 K (25 °c and 250 °c). *Metall Mater Trans A Phys Metall Mater Sci*. 2014;45:3254-3274.
9. Wang L, Huang Z, Wang H, et al. Study of slip activity in a Mg-Y alloy by in situ high energy X-ray diffraction microscopy and elastic viscoplastic self-consistent modeling. *Acta Mater*. 2018;155:138-152.
10. Withers PJ, Bouman C, Carmignato S, et al. X-ray computed tomography. *Nat Rev Methods Primers*. 2021;1(18):1-21.
11. Menasche DB, Shade PA, Safriet S, Kenesei P, Park JS, Musinski WD. Deep learning approaches to semantic segmentation of fatigue cracking within cyclically loaded nickel superalloy. *Comput Mater Sci*. 2021;198:110683.
12. Wu SC, Xiao TQ, Withers PJ. The imaging of failure in structural materials by synchrotron radiation X-ray microtomography. *Eng Fract Mech*. 2017;182:127-156.
13. King A, Johnson G, Engelberg D, Ludwig W, Marrow J. Observations of intergranular stress corrosion cracking in a grain-mapped Polycrystal. *Science*. 2008;321(5887):382-385.
14. Gustafson S, Ludwig W, Shade P, et al. Quantifying microscale drivers for fatigue failure via coupled synchrotron X-ray characterization and simulations. *Nat Commun*. 2020;11(1):1-10.
15. Lienert U, Li SF, Hefferan CM. High-energy diffraction microscopy at the advanced photon source. *Jom*. 2011;63(7):70-77.
16. Poulsen HF. An introduction to three-dimensional X-ray diffraction microscopy. *J Appl Cryst*. 2012;45(6):1084-1097.
17. Ludwig W, Reischig P, King A, et al. Three-dimensional grain mapping by x-ray diffraction contrast tomography and the use of Friedel pairs in diffraction data analysis. *Rev Sci Instrum*. 2009;80(3):033905.
18. Herbig M, King A, Reischig P, et al. 3-D growth of a short fatigue crack within a polycrystalline microstructure studied using combined diffraction and phase-contrast X-ray tomography. *Acta Mater*. 2011;59(2):590-601.
19. King A, Ludwig W, Herbig M, et al. Three-dimensional in situ observations of short fatigue crack growth in magnesium. *Acta Mater*. 2011;59(17):6761-6771.
20. Oddershede J, Camin B, Schmidt S, et al. Measuring the stress field around an evolving crack in tensile deformed Mg AZ31 using three-dimensional X-ray diffraction. *Acta Mater*. 2012;60(8):3570-3580.
21. Spear AD, Li SF, Lind JF, Suter RM, Ingraffea AR. Three-dimensional characterization of microstructurally small fatigue-crack evolution using quantitative fractography combined with post-mortem X-ray tomography and high-energy X-ray diffraction microscopy. *Acta Mater*. 2014;76:413-424.
22. Naragani DP, Shade PA, Kenesei P, Sharma H, Sangid MD. X-ray characterization of the micromechanical response ahead of a propagating small fatigue crack in a Ni-based superalloy. *Acta Mater*. 2019;179:342-359.
23. Naragani D, Sangid MD, Shade PA, et al. Investigation of fatigue crack initiation from a non-metallic inclusion via high energy x-ray diffraction microscopy. *Acta Mater*. 2017;137:71-84.
24. Ravi P, Naragani D, Kenesei P, Park JS, Sangid MD. Direct observations and characterization of crack closure during microstructurally small fatigue crack growth via in-situ high-energy X-ray characterization. *Acta Mater*. 2021;205:116564.
25. Hanson JP, Bagri A, Lind J, et al. Crystallographic character of grain boundaries resistant to hydrogen-assisted fracture in Ni-base alloy 725. *Nat Commun*. 2018;9(1):3386.
26. Ganesan S, Yaghoobi M, Githens A, et al. The effects of heat treatment on the response of WE43 Mg alloy: crystal plasticity finite element simulation and SEM-DIC experiment. *Int J Plast*. 2021;137:102917.
27. Adams JF, Allison JE, Jones JW. The effects of heat treatment on very high cycle fatigue behavior in hot-rolled WE43 magnesium. *Int J Fatig*. 2016;93:372-386.
28. Githens AS. Deformation mechanisms of magnesium alloy WE43 under monotonic tensile loading. M.S. thesis, 2015.

29. Adams JF. Investigating microstructural effects on short crack growth and fatigue life behavior of WE43 magnesium. Ph. D dissertation, 2018.
30. Geathers J, Torbet CJ, Jones JW, Daly S. Investigating environmental effects on small fatigue crack growth in Ti-6242S using combined ultrasonic fatigue and scanning electron microscopy. *Int J Fatig*. 2015;70:154-162.
31. Mayer H. Recent developments in ultrasonic fatigue. *Fatigue Fract Eng Mater Struct*. 2016;39(1):3-29.
32. Willertz LE. Ultrasonic fatigue. *Int Mater Rev*. 1980;25(1):65-78.
33. Li SF, Suter RM. Adaptive reconstruction method for three-dimensional orientation imaging. *J Appl Cryst*. 2013;46(2):512-524.
34. Sharma H, Huizenga RM, Offerman SE. A fast methodology to determine the characteristics of thousands of grains using three-dimensional X-ray diffraction. I. Overlapping diffraction peaks and parameters of the experimental setup. *J Appl Cryst*. 2012;45(4):693-704.
35. Sharma H, Huizenga RM, Offerman SE. A fast methodology to determine the characteristics of thousands of grains using three-dimensional X-ray diffraction. II. Volume, Centre-of-mass position, crystallographic orientation and strain state of grains. *J Appl Cryst*. 2012;45(4):705-718.
36. Phung BR, Greeley DA, Yaghoob M, Adams JF, Allison JE, Spear AD. Predicting microstructurally sensitive fatigue-crack path in WE43 magnesium using high-fidelity numerical modeling and three-dimensional experimental characterization. *Fatigue Fract Eng Mater Struct*. 2023. doi:https://doi.org/10.1111/ffe.14210
37. Bachmann F, Hielscher R, Schaeben H. Texture analysis with MTEX—free and open source software toolbox. *Solid State Phenom*. 2010;160:63-68.
38. Luster J, Morris MA. Compatibility of deformation in two-phase Ti-Al alloys: dependence on microstructure and orientation relationships. *Metall Mater Trans A*. 1995;26(7):1745-1756.
39. Pedregosa F, Michel V, Grisel O, et al. Scikit-learn: machine learning in Python. *J Machine Learn Res*. 2011;12:2825-2830.
40. Pisner DA, Schnyer DM. Support vector machine. In: *Machine Learning: Methods and Applications to Brain Disorders*; 2020:101-121.
41. Noble WS. What is a support vector machine? *Nat Biotechnol*. 2006;24(12):1565-1567.
42. Marrow TJ, Mostafavi M, Hashimoto T, Thompson GE. A quantitative three-dimensional in situ study of a short fatigue crack in a magnesium alloy. *Int J Fatigue*. 2014;66:183-193.
43. Kacher J, Eftink BP, Cui B, Robertson IM. Dislocation interactions with grain boundaries. *Curr Opin Solid State Mater Sci*. 2014;18(4):227-243.
44. Jiang S, Jia Y, Wang X. In-situ analysis of slip transfer and heterogeneous deformation in tension of Mg-5.4Gd-1.8Y-1.5Zn alloy. *J Magnes Alloys*. 2020;8(4):1186-1197.
45. Wang H, Boehlert CJ, Wang QD, Yin DD, Ding WJ. In-situ analysis of the slip activity during tensile deformation of cast and extruded Mg-10Gd-3Y-0.5Zr (wt.%) at 250°C. *Mater Charact*. 2016;116:8-17.
46. Zhou B, Li Y, Wang L, Jia H, Zeng X. The role of grain boundary plane in slip transfer during deformation of magnesium alloys. *Acta Mater*. 2022;227:117662.
47. Zhai T, Wilkinson AJ, Martin JW. A crystallographic mechanism for fatigue crack propagation through grain boundaries. *Acta Mater*. 2000;48(20):4917-4927.
48. Panwar S, Adams JF, Allison JE, Jones JW, Sundararaghavan V. A grain boundary interaction model for microstructurally short fatigue cracks. *Int J Fatig*. 2018;113:401-406.
49. Gao Y, Stölken JS, Kumar M, Ritchie RO. High-cycle fatigue of nickel-base superalloy René 104 (ME3): interaction of microstructurally small cracks with grain boundaries of known character. *Acta Mater*. 2007;55(9):3155-3167.
50. Li L, Zhang Z, Zhang P, Zhang Z. A review on the fatigue cracking of twin boundaries: crystallographic orientation and stacking fault energy. *Prog Mater Sci*. 2023;131:101011.
51. Randle V. Twinning-related grain boundary engineering. *Acta Mater*. 2004;52(14):4067-4081.
52. Bhattacharyya JJ, Wang F, McQuade PJ, Agnew SR. Deformation and fracture behavior of mg alloy, WE43, after various aging heat treatments. *Mater Sci Eng A*. 2017;705:79-88.
53. Srivastava S, Yaghoobi M, Sundararaghavan V. A graph-theoretic approach for multiscale modeling and prediction of crack propagation in polycrystalline materials. *Eng Fract Mech*. 2021;241:107406.
54. Suresh S, Ritchie RO. A geometric model for fatigue crack closure induced by fracture surface roughness. *Metall Trans A*. 1982;13(9):1627-1631.
55. Pippan R, Hohenwarter A. Fatigue crack closure: a review of the physical phenomena. *Fatigue Fract Eng Mater Struct*. 2017;40(4):471-495.
56. Künkler B, Düber O, Köster P, Krupp U, Fritzen CP, Christ HJ. Modelling of short crack propagation—transition from stage I to stage II. *Eng Fract Mech*. 2008;75(3–4):715-725.

How to cite this article: Greeley DA, Adams JF, Kenesei P, Spear AD, Allison JE. Quantitative analysis of three-dimensional fatigue crack path selection in Mg alloy WE43 using high-energy X-ray diffraction microscopy. *Fatigue Fract Eng Mater Struct*. 2024;1-22. doi:10.1111/ffe.14217